



Global clear-sky surface skin temperature from multiple satellites using a single-channel algorithm with viewing zenith angle correction

Benjamin R. Scarino¹, Patrick Minnis², Thad Chee¹, Kristopher M. Bedka², Christopher R. Yost¹, and Rabindra Palikonda¹

5 ¹Science Systems and Applications, Inc., One Enterprise Pkwy Ste 200, Hampton, VA 23666 USA

²NASA Langley Research Center, 21 Langley Blvd MS 420, Hampton, VA 23681-2199 USA

Correspondence to: Benjamin R. Scarino (benjamin.r.scarino@nasa.gov)

Abstract. Surface skin temperature (T_s) is an important parameter for characterizing the energy exchange at the ground/water-atmosphere interface. The Satellite CIOud and Radiation Property retrieval System (SatCORPS) employs a single-channel thermal-infrared- (TIR-) method to retrieve T_s over clear-sky land and ocean surfaces from data taken by geostationary-Earth orbit (GEO) satellite and low-Earth orbit (LEO) satellite imagers. GEO satellites can provide somewhat continuous estimates of T_s over the diurnal cycle in non-polar regions, while polar T_s retrievals from LEO imagers, such as the Advanced Very High Resolution Radiometer (AVHRR) can complement the GEO measurements. The combined global coverage of remotely sensed T_s , along with accompanying cloud and surface radiation parameters, produced in near-real time and from historical satellite data, should be beneficial for both weather and climate applications. For example, near-real-time hourly T_s observations can be assimilated in high-temporal resolution numerical weather prediction models and historical observations can be used for validation or assimilation of climate models. Key drawbacks to the utility of TIR-derived T_s data include the limitation to clear-sky conditions, the reliance on a particular set of analyses/reanalyses necessary for atmospheric corrections, and the dependence on viewing angle. Therefore, T_s validation with established references is essential, as is proper evaluation of T_s sensitivity to atmospheric correction source.

This article presents improvements on the NASA Langley GEO satellite and AVHRR TIR-based T_s product, derived using a single-channel technique. The resulting clear-sky skin temperature values are validated with surface references and independent satellite products. Furthermore, an empirical means of correcting for the viewing-angle dependency of satellite land surface temperature (LST) is explained and validated. Application of a daytime nadir-normalization model yields improved accuracy and precision of GOES-13 LST relative to independent Moderate-resolution Imaging Spectroradiometer (MYD11_L2) LST and Atmospheric Radiation Measurement Program/NOAA ESRL Surface Radiation network ground stations. These corrections serve as a basis for a means to improve satellite-based LST accuracy, thereby leading to better monitoring and utilization of the data. The immediate availability and broad coverage of these skin temperature observations should prove valuable to modelers and climate researchers looking for improved forecasts and better understanding of the global climate model.

30 **1 Introduction**

Surface skin temperature (T_s) is a critical quantity for characterizing the exchange of energy between the Earth's surface and the atmosphere. Consistent land and ocean measurements of T_s are essential for regional and global climate assessment and weather model data assimilation. Surface energy balance and top-of-atmosphere (TOA) radiative budget calculations rely on the accuracy of these surface parameters (Bodas-Salcedo et al., 2008). In addition to surface flux analyses, T_s retrievals are used to minimize model prediction uncertainty by updating model state values with observations at regular time steps – an important consideration for climate and numerical weather prediction (NWP) models (Garand, 2003; Tsuang et al., 2008; Reichle et al.,



2010; Ghent et al. 2010; Guillevic et al., 2012; Draper et al., 2014). The modeling community could benefit significantly from the provision of frequent, spatially contiguous, global land and ocean T_s data (Rodel et al. 2004, Bosilovich et al. 2007). Many other uses of T_s as well as the status and future of T_s retrievals are summarized by Li et al. (2013). It is clear that the need is growing for higher accuracy, global coverage, and greater temporal and spatial resolution of T_s retrievals from satellite imager data.

5

Satellite-based T_s retrieval, validation, and modeling studies originate from a variety of sources, e.g., the National Environmental Satellite, Data, and Information Service (NESDIS) and the National Oceanic and Atmospheric Administration (NOAA) via the Advanced Very High Resolution Radiometer (AVHRR) series and the Geostationary Operational Environmental Satellite (GOES) sensors (Prata, 1993, 1994; Coll and Caselles, 1997; Sobrino and Raissouni, 2000; Kerr et al., 2004; Sobrino et al., 2004; Yu et al., 2009, 2010, 2012; Sun et al., 2012). Specifically, using a single-channel land surface temperature (LST) algorithm, Heidinger et al. (2013) found good agreement with ground sources in a verification study of GOES and AVHRR Pathfinder Atmospheres–Extended (PATMOS-x) LST. Furthermore, near-real-time LST is produced operationally from Meteosat Spinning Enhanced Visible and Infrared Imager (SEVIRI) data, which offer continuous coverage of Europe and Africa, and served as the focus of several LST validation studies (DaCamara, 2006; Kabsch et al., 2008; Trigo et al., 2008; Göttsche et al., 2013). Retrievals using radiances from the Moderate Resolution Imaging Spectroradiometer (MODIS) have been both the target and standard for a number of LST verification studies (Wan et al., 2002, 2004, 2008; Coll et al., 2009; Jiménez et al., 2012). Duan et al. (2014) used four daily observations from Terra- and Aqua-MODIS to capture the diurnal cycle of LST, which is critical for full characterization of the climate system. Wang et al. (2014) conducted a three-way T_s comparison using MODIS, in situ ground observations, and model simulations. They note the high importance of accurate cloud-clearing and the inherent difficulties of resolution scaling when comparisons are conducted between satellite data and point references – conclusions supported in a similar MODIS daytime LST verification study conducted by Williamson et al. (2013).

10

15

20

With more reliable calibrations, operational GEO and low Earth-orbiting (LEO) satellite imagers are being used to derive cloud and radiation properties in near real time (NRT), e.g., Minnis et al. (2008a). The combination of GOES-East (GOES-13), GOES-West (GOES-15), Meteosat Second Generation (MSG; Meteosat-9 or Meteosat-10), MTSAT-2 (recently replaced by Himawari-8), and the Indian Space Research Organization INSAT-3D provides high-temporal resolution (1-hour nominal) quasi-global T_s data produced in NRT, with a shared single-channel retrieval algorithm (e.g., Fig. 1). The methodology (Section 2) is flexible and easily transportable to other GEO and LEO imagers, including the current AVHRR instruments on the NOAA and EUMETSAT MetOp platforms. Near-real-time AVHRR T_s retrievals supplement the GEO data and fill in missing measurements over polar regions (e.g., Fig. 2). This same method is being applied to historic and current imager datasets, particularly as part of the Satellite Cloud and Radiative Property retrieval System (SatCORPS) analyses of AVHRR data for provision of a NOAA Climate Data Record (Minnis et al., 2016), and for MODIS, GEO, and Suomi-National Polar-Orbiting Partnership (S-NPP) Visible Infrared Imaging Radiometer Suite data as part of the Clouds and Earth's Radiant Energy System (CERES) project (e.g., Minnis et al., 2010).

25

30

This article highlights recent improvements made to the SatCORPS NRT satellite T_s product (Scarino et al., 2013), via comparisons of GOES and AVHRR T_s retrievals with established sea surface temperature (SST; Section 4) and LST (Section 5) reference datasets. The influence of NWP source on retrieved T_s values is also examined. The main improvements over the earlier version are enhanced pixel-level resolution output and hourly GEO retrieval time steps. The SatCORPS T_s retrieved from GOES and AVHRR data are evaluated by comparing with reference datasets based on in situ, surface, and satellite measurements. In addition to the validation comparisons, an empirical means of correcting for LST viewing angle dependency is developed and tested against the reference datasets. The combined GEO and AVHRR retrievals allow for high-resolution

40



temporal monitoring of the T_s diurnal cycle, an essential state variable for numerical weather model data assimilation and climate studies (e.g., Draper et al., 2014). The T_s products and uncertainties described here should be valuable for improving surface energy flux analyses and numerical weather prediction owing to their NRT global availability over land and ocean.

2 Data

5 2.1 Satellite data for surface skin temperature retrieval

Clear-sky surface skin temperature is retrieved from channel 4 (11 μm) radiances taken by the NOAA-18 AVHRR for the period January–December 2008 in the Global Area Coverage (GAC) format. The nominal satellite equatorial crossing time is 13:30 LT during that time period. A GAC pixel radiance is formed by averaging the radiances of four consecutive raw 1-km AVHRR pixels along the scan direction. The process is repeated after skipping the fifth pixel and so on to produce consecutive GAC pixels along the scan line. Two scan lines are then skipped and the pixel averaging is applied again to the third scan line. Thus, a GAC pixel nominally covers a 1-km \times 4-km area (a 2 km² pixel), but because of sampling, represents a 3-km \times 5-km area that yields an effective resolution of \sim 4 km. The AVHRR data were analyzed with the SatCORPS-A1 methodology (Minnis et al., 2016) to retrieve cloud properties, TOA broadband fluxes, and clear-sky surface skin temperature. Clear pixels are determined from the SatCORPS cloud mask. Details of the skin temperature retrieval process are given in Section 3.

10
15
20
Hourly channel-4 (10.8 μm) data from GOES-13 (GOES-East) and GOES-15 (GOES-West) taken during January, April, July, and October (hereafter, JAJO) 2013 are used to retrieve T_s for validation with surface and other satellite surface skin temperature datasets. Furthermore, GOES-13 and GOES-15 data are employed to test the viewing angle correction parameterization. The nominal GOES imager resolution is 4 km. The pixels are sub-sampled, however, to an effective resolution of 8-km during full disk and hourly hemispheric scans. These data were analyzed with a version of SatCORPS-A1 adapted to the GOES channels as described by Minnis et al. (2008a).

Aqua-MODIS data taken over the GOES-East domain were analyzed with the CERES Ed4 retrieval code (Minnis et al., 2008b, 2010, 2011) to match with the GOES-13 LST retrievals during JAJO 2013. The matched data are used to develop a parameterization to correct LST for viewing zenith angle (VZA) dependence. The MODIS data are taken twice per day at a 1-km resolution within 1.5 hours of \sim 0130 and 1330 LT.

25 2.2 Validation data

For validation comparisons, this study employs surface and satellite-based references. The SatCORPS AVHRR SST values are compared to the daily high-resolution blended SST analysis described by Reynolds et al. (2007). It comprises the NOAA “Optimum Interpolation” SST (OI SST) Version-2 high-resolution dataset, which consists of a global 0.25° \times 0.25° grid of blended satellite (AVHRR two- and three-channel algorithms) and in situ measurements of daily SST. It covers the period from
30 January 1981 to the present.

Surface radiometer measurements are used to validate the SatCORPS AVHRR and GOES LST values. Two surface datasets are employed: the NOAA ESRL Surface Radiation (SURFRAD) network upwelling/downwelling Eppley hemispheric Precision Infrared Radiometer (PIR) broadband longwave fluxes (Augustine et al., 2000), and the Atmospheric Radiation Measurement (ARM) Southern Great Plains (SGP) Central Facility (36.3°N, 97.5°W) 11- μm upwelling/downwelling infrared thermometer (IRT) brightness temperatures (Morris, 2006). Both datasets are common references for evaluating LST retrievals over the
35 contiguous United States (Guillevic et al., 2012; Yu et al., 2012; Heidinger et al., 2013; Wang et al., 2014).



The ARM IRT ground-based radiation pyrometers provide measurements of the equivalent blackbody brightness temperature for the 9.6-11.5- μm spectral band every 60 seconds. From a 10-meter-height with 30.5° FOV, the upwelling IRT measures the effective ground radiating temperature, i.e., the temperature equivalent of the ground infrared radiant energy assuming the surface emissivity (ε_s) is equal to 1.0 (Morris 2006). A true skin temperature T_s can, therefore, be determined as

$$T_s = B^{-1} \left\{ \frac{B(T_o) - (1 - \varepsilon_s) \times B(T_{o\downarrow})}{\varepsilon_s} \right\}, \quad (1)$$

where ε_s is from the CERES 11- μm database (e.g., Chen et al., 2004) and the spectral downwelling narrowband brightness temperature ($T_{o\downarrow}$), which is measured by a 2-meter-height up-looking IRT. The Planck function for the particular waveband is $B(T)$, and T_o is temperature equivalent to the surface-leaving blackbody radiance. Note that the ARM downwelling IRT at the Lamont, OK Central Facility was no longer operating in 2013, therefore $T_{o\downarrow}$ was acquired from the nearby Lamont, OK Extended Facility downwelling IRT, which operates in unison with the Central Facility instrument. It is expected that there is negligible variation in $T_{o\downarrow}$ over the ~200-m distance between the two sites.

The SURFRAD network currently consists of seven stations situated in geographically diverse regions across the continental United States. At each station, two PIRs measure the upwelling and downwelling broadband longwave thermal infrared irradiance (LW_{\uparrow} and LW_{\downarrow}) in the spectral range from 3.0 to 50.0 μm every 60 seconds (every 180 seconds in 2008). Surface skin temperature is determined from LW_{\uparrow} and LW_{\downarrow} by

$$T_s = \left[\frac{LW_{\uparrow} - (1 - \varepsilon_B) \times LW_{\downarrow}}{\varepsilon_B \times \sigma} \right]^{1/4}, \quad (2)$$

where ε_B is the CERES broadband emissivity (Wilber et al., 1999) and σ is the Stefan-Boltzmann constant.

Another LST reference dataset used here is the Version-5 Aqua-MODIS LST/Emissivity product (MYD11_L2; hereafter, MYD11), which is derived from the generalized split-window algorithm (Wan and Dozier 1996; Wan and Li, 1997; Snyder and Wan, 1998). It includes values of LST and surface spectral emissivity values retrieved from clear-sky 1-km MODIS pixels. Because MYD11 is derived from different data using a different type of algorithm, and is accurate to ± 1 K or less (Wan et al., 2002, 2004; Wan, 2008), it serves well as an independent reference for comparing with the GOES retrievals.

2.3 Reanalysis input

Model data are used as input to compute TOA brightness temperatures (T_{toa}). These include the model surface air (T_a) and skin (T_s') temperatures, and vertical temperature and humidity profiles. The real-time GEO retrievals employ National Centers for Environmental Prediction (NCEP) Global Forecast System (GFS; EMC, 2003) model forecasts accessed from the Man-computer Interactive Data Analysis System (McIDAS; Lazzara et al. 1999). Non-real-time GEO studies utilize either GFS or Modern-Era Retrospective Analysis for Research and Applications (MERRA; Reinecker *et al.*, 2011) reanalyses. The impacts of using one reanalysis or the other are examined by analyzing the same satellite data using each of the two reanalyses during the T_s retrieval.

MERRA data have a spatial resolution of 0.5° latitude \times 0.66° longitude over the globe. The surface skin temperature is available hourly, while the temperature and humidity profiles are provided every 6 hours. A total of 43 atmospheric layers are used. The version of GFS used here has a 1.25° horizontal resolution and up to 11 levels in the vertical, and provides data every 6 hours. No model values of T_s' are available in the GFS version over land, so T_s' is estimated from T_a as a function of local time and season.



3 Single-channel skin temperature retrieval

The method for calculating T_s from 11- μm T_{toa} observations is an updated, higher-resolution version of that described by Scarino et al. (2013). Because some imagers (e.g., AVHRR-1, GOES-13) lack split-window capabilities, the single-channel method best allows historical consistency in application amongst many distinct sensors (Sun and Pinker, 2003; Jiménez-Muñoz and Sobrino, 2010; Heidinger, 2013). The analysis employs the cloud mask algorithm developed for the Clouds and the Earth's Radiant Energy System (CERES) to classify pixels as cloudy or clear on a chosen grid (Minnis et al. 2008b). The algorithm relies on comparisons of observations with estimates of the clear-sky T_{toa} or reflectance at 0.65, 3.8, and 10.8 μm . Those estimates are made using the CERES 10' clear-sky albedo and land surface emissivity databases (Chen et al., 2004, 2010), along with the appropriate bidirectional and directional reflectance models, angularly dependent sea surface emissivity models, predicted skin temperature, and corrections for atmospheric absorption and emission (Minnis et al., 2011). The emissivity for water surfaces is estimated using a wind-speed-dependent model developed from theoretical calculations using the approach of Jin et al. (2006). A constant wind-speed of 5 knots is assumed for all pixels.

The observed or modeled radiance at the TOA can be represented as:

$$B(T_{TOA}) = \prod_{i=n}^1 t_i [B(T_o)] + (1 - t_1)B(T_1) + \sum_{i=n}^2 (1 - t_i)B(T_i) \prod_{j=i}^1 t_j, \quad (3)$$

where T_o is the surface-leaving radiant energy equivalent brightness temperature, which comes from T_s based on the following relationship using the narrowband surface emissivity:

$$T_s = B^{-1} \left\{ \frac{[B(T_o) - (1 - \epsilon_s) \times L_{\downarrow}]}{\epsilon_s} \right\}, \quad (4)$$

where L_{\downarrow} is the downwelling radiant energy at the surface:

$$L_{\downarrow} = (1 - t_n)B(T_n) + \sum_{i=1}^{n-1} (1 - t_i)B(T_i) \prod_{j=n}^{i+1} t_j, \quad (5)$$

The subscripts i and j denote an atmospheric layer, where 1 and n refer to the layers at the TOA and just above the surface, respectively [e.g., $B(T_i) \equiv B(T_{toa})$]. The atmospheric layer temperature is T_i , and B is evaluated at the central wavelength of the 11- μm band. B^{-1} is the inverse Planck function. The layer transmissivity (t_i) derives from the correlated k -distribution technique. This technique is described in detail by Goody et al. (1989) and Kratz (1995), which depict the discrete version of the spectral-mean transmission $t_{\omega}(u, p, \theta)$ as:

$$t_{\omega}(u, p, \theta) \equiv \sum_{i=1}^n w_i \exp[-k_i(p, \theta)u], \quad (6)$$

where $k_i(p, \theta)$ is an absorption coefficient as a function of pressure p and temperature θ for a particular wavenumber ω , u is a pathlength, and w_i is a weighting factor for which the summation over n calculations must equal 1.

The surface temperatures and atmospheric profiles are linearly interpolated temporally to the satellite image time and spatially to the center of each $0.5^{\circ} \times 0.5$ AVHRR or $1.0^{\circ} \times 1.0^{\circ}$ GEO region. In the case of AVHRR retrievals, regions can have resolutions up to $1.5^{\circ} \times 1.5^{\circ}$ near the poles, but are nominally $0.5^{\circ} \times 0.5^{\circ}$ everywhere else. The same T_s retrieval methodology is used for all resolutions. The specific logic of the cloud mask algorithm can be found in Minnis et al. (2008a, 2010, 2016) and Trepte et al. (2010), which describe cloud tests for different scenarios (e.g., scenes over snow or desert, sun-glint-influenced ocean, scenes with smoke or thin cirrus). It is important to note that although the NWP skin temperature T_s' is used as a seed value in the initial application of the cloud mask, decisions based solely on the difference between 11- μm observations and model values occur for only 2.3% (5.3%) of the pixels over land during the day (night). Therefore, the initial influence T_s' is significantly diminished.



After the cloud mask is applied, the mean 0.65- μm reflectance and 3.8- and 10.8- μm T_{toa} (i.e., $\langle T_{toa} \rangle$) values are computed from the clear and cloudy pixels for each region. The data are then analyzed as 8×12 -pixel tiles for AVHRR or $1.0^\circ \times 1.0^\circ$ regions for GEO. If at least 20% of the pixels within the tile or region are considered clear, the mean observed clear-sky temperature replaces the original NWP-based clear-sky temperature for the region and the cloud mask is repeated using the observed clear-sky mean brightness temperature. The 20% criterion is used to minimize the influence of cloudy pixels on the final temperature value while still allowing sufficient sample size. If fewer than 20% of the pixels are clear, then the original clear-sky estimate T_s' and cloud mask are retained and no value T_s is retrieved.

5

For those tiles/regions satisfying the 20% criterion, a value of T_s for each pixel is determined using a two-step process. First, the tile/regional mean value T_s (i.e., $\langle T_s \rangle$) is determined by solving Eq (3) from the inverse of Eq (4) (i.e., T_o' solved from T_s'), and then using the mean observed 11- μm clear-sky $\langle T_{toa} \rangle$ to adjust T_s' based on the difference between the $\langle T_{toa} \rangle$ and the modeled T_{toa}' for each tile/region. That is, a correction is applied to the model T_s' and temperature/humidity profiles such that T_{toa}' computed with Eqs (3) and (4) equals $\langle T_{toa} \rangle$, thereby yielding $\langle T_s \rangle$. For the AVHRR retrievals, $\langle T_{toa} \rangle$ represents a tile value, whereas T_{toa}' represents the larger regional value because the latter originates from the region-scale MERRA T_s' . Thus, all tiles having their center within a given MERRA grid box use the same model profiles and T_s' . For the GEO T_s retrieval, both the observed $\langle T_{toa} \rangle$ and the modeled T_{toa}' are represented on the $1.0^\circ \times 1.0^\circ$ region scale.

10

15

To save computational time, a value of T_s is estimated for each pixel in the tile or region as

$$T_s = B^{-1} \left[R_T B(T_{TOA}) \right], \quad (7)$$

where R_T is the ratio

$$R_T = \frac{B(\langle T_s \rangle)}{B(\langle T_{TOA} \rangle)}, \quad (8)$$

20

and T_{toa} is the observed clear-sky brightness temperature for the pixel. This approach yields T_s pixel values that differ by -0.04 ± 0.20 K from the $\langle T_s \rangle$ computed using Eqs (3) and (4).

4. Sea surface temperature validation

Sea surface temperatures were retrieved as described above for the 2008 AVHRR datasets and are compared with the OI SST values. The AVHRR SST pixel data were first gridded to match the NOAA OI SST 0.25° resolution. Only those pixels classified as clear, with 100% water fraction (based on a $1.0^\circ \times 1.0^\circ$ land mask) and 0% sea ice fraction outside of sun-glint conditions were used to compute the daily grid averages. Additionally, each pixel must be assigned a quality assurance flag of 1, indicating that there are no adjacent cloudy pixels or nearby thin cirrus (within two pixels).

25

Figure 3 maps the July 2008 SST means from AVHRR (Fig. 3a) and NOAA OI SST (Fig. 3b), and their differences (Fig. 3c), which qualitatively reveal very good agreement between the two products. The Fig. 3d scatter density plot reveals a more quantitative analysis of the ~ 3 million daily, cell-to-cell comparisons. The bias and standard deviation of the difference (SDD) of the AVHRR SST relative to OI SST for July 2008 are -0.06 K and 0.62 K, respectively. A high associated coefficient of determination ($R^2 > 0.99$; not shown) indicates low variance, despite apparent outliers. Disagreements over open ocean, such as those in the tropical western Pacific and northern Pacific Ocean, can be attributed to cloud-clearing differences between the two products, or to the fact that the OI satellite SST is supplemented by in situ measurements from buoys and ships that are free of cloud consideration. Nevertheless, despite localized coastal differences and cloud influences, the AVHRR SST is largely consistent with the NOAA OI SST product.

30

35



Sea surface temperatures from JAJO 2013 GOES-13 are compared to NOAA OI SSTs under the same gridding, filtering, and quality assurance criteria used for the AVHRR comparisons. Whereas the AVHRR SST retrievals always utilize atmospheric corrections based on MERRA reanalysis, the GEO SST retrievals utilize either GFS or MERRA for the atmospheric corrections. The near-real-time GEO retrievals currently rely on GFS forecasts, whereas the MERRA reanalysis is suitable for historical GEO and AVHRR retrievals. Therefore, it is important to quantify the influence of the particular NWP reanalysis on satellite-based SST retrieval. Figure 4 compares the July 2013 GOES-13 SSTs retrieved using the GFS-based atmospheric corrections. The GOES SSTs are rather poor in both accuracy and precision relative to the reference – an absolute bias approaching -0.7 K with SDD = 1.02 K. These significant increases in bias and SDD can be attributed to the difference in NWP source, as is evident from Fig. 5. Figure 5 shows the same comparison as Fig. 4, except that MERRA profiles were used for the atmospheric corrections. Similar then to the AVHRR retrievals, MERRA-derived GOES-13 SSTs exhibit a near-zero bias and an SDD of only 0.60 K relative to the NOAA OI SST reference.

The accuracy and precision of the GFS- and MERRA-derived GOES-13 SST values for the remaining seasonal months of 2013 are illustrated in Fig. 6 along with their AVHRR counterparts for all 12 months of 2008. Mean AVHRR SST is consistently 0.1-K, or less, colder than the NOAA OI SST reference throughout the year. The AVHRR SST monthly SDD is steady near 0.6 K. The MERRA-based JAJO GOES-13 SST SDD is also steady near 0.6 K and the bias is consistently close to zero. The differences between the AVHRR and GOES biases are likely due to uncertainties in the infrared calibrations. The GFS-derived GOES-13 mean SST is consistently ~0.6 K colder than the NOAA reference, with an SDD in excess of 1.0 K for the JAJO seasonal months. This discrepancy with the MERRA-based results suggests that the GFS model profiles are drier than MERRA and/or have insufficient vertical resolution to properly account for the changes in water vapor that are used to compute the atmospheric attenuation of the infrared radiation. It is unlikely that the GFS humidity is too low since it appears to have a wet bias (Yoo, 2012). An explanation for the differences in the model fields is beyond the scope of this paper. However, it is clear that the single-channel retrieval method is sensitive to the source of temperature and humidity profiles. Hereafter, the MERRA data are used for all analyses, unless indicated otherwise.

5. Land surface temperature viewing angle dependency correction

Satellite-observed LST depends on the viewing and illumination conditions because shading, vegetation conditions, soil type, and topography affect the radiance exiting the scene (Lagouarde et al., 1995; Minnis and Khaiyer 2000; Minnis et al. 2004). This thermal radiation anisotropy can result in the retrieved LST varying by 6 K or more for some areas (Rasmussen et al., 2010, 2011; Guillevic. et al. 2013). From experimental measurements, Sobrino and Cuenca (1999) and Cuenca and Sobrino (2004) found a VZA dependence of LST that depends on soil type. Pinheiro et al. (2006) developed a physical model to estimate the variation of LST as a function of canopy coverage, solar zenith angle (SZA), VZA, and relative azimuth angle (RAA) for a savanna. Rasmussen et al. (2010, 2011) developed and applied a similar model to predict the LST that would be retrieved by Meteosat over Africa. Vinnikov et al. (2012) constructed a generalized model to correct for all angles, but, for general application, it requires many sets of matched measurements from different angle sets to construct the necessary kernels. Addressing the anisotropic effects, and thereby leading to more accurate interpretation of T_s , can not only improve climate studies, but can also be of significant benefit to data assimilation and numerical weather prediction needs (Reichle et al., 2010; Guillevic et al., 2013; Draper et al., 2014).

Accounting for 3-D radiance anisotropy for a global retrieval methodology will require the development of regional and seasonal kernels for a universal model (e.g., Vinnikov et al. 2012) or developing canopy configurations globally for physical models (e.g.,



Rasmussen et al. 2010). In lieu of developing a comprehensive model that accounts for all three angles, a simple empirical model is developed in this section to account for the average dependence of the retrieved LST values on VZA. Although this initial step toward a universally applicable model provides correction for only one component of the anisotropy, it reduces the uncertainty of the retrieved LST values, as shown below.

5 5.1. Nadir-Normalization Model

The VZA correction model relies on simultaneous matched LST values from GOES-13 and Aqua-MODIS. Land surface temperature is retrieved from MODIS using the same single-channel methodology described in Section 2. Hourly JAJO 2013 GOES-13 and twice-daily Aqua-MODIS LST values were first averaged on a $1.0^\circ \times 1.0^\circ$ grid encompassing 60°N to 60°S and 120°W to 30°W . For each MODIS overpass, the MODIS LST means of each gridbox were matched with their GOES counterparts whenever the sampling times differed by less than 30 minutes. The GOES-East satellite was chosen to build the empirical model given the abundance of landmass in both the northern and southern hemispheres within the sensor field of view (FOV). The bulk of the higher VZAs, however, is concentrated in North America as the South American landmass dwindles south of 20°S . It is assumed that the VZA correction based on the GOES-East model will yield similar improvements when applied to LST retrievals from other satellites.

The MODIS LST retrievals limited to views having cosine(VZA), or $CVZA$, greater than $D=0.95$ serve as the nadir LST reference at all GOES-East viewing angles. That is, GOES-13-minus-MODIS mean LST biases are computed for intervals of VZA difference (ΔVZA), expressed, however, in terms of cosine(ΔVZA), or $CAVZA$, intervals. Here, because the MODIS data are from near-nadir views, $CAVZA$ and $CVZA$ are essentially interchangeable. The empirical relationship is illustrated in Fig. 7 for daytime LST matches during the JAJO seasonal months. The ΔVZA interval step is 1° , increasing from a starting point of $\Delta VZA = 15^\circ$. In an effort to effect gradual, stable change in bias with respect to $CAVZA$, a $CAVZA$ allowance (A) was employed at each $CAVZA$ interval (I) as follows:

$$A(I) = 0.5 \left[\left(ID + \sqrt{(1-I^2)(1-D^2)} \right) - \left(ID - \sqrt{(1-I^2)(1-D^2)} \right) \right], \quad (9)$$

which derives from

$$A(\Delta VZA) = 0.5 \left[\cos(\Delta VZA - \cos^{-1}(D)) - \cos(\Delta VZA + \cos^{-1}(D)) \right] \quad (10)$$

Thus, the mean bias (Fig. 7 solid black dots) is determined at each $CAVZA$ interval I for matched GOES-13 and MODIS LST pairs for which the satellite $CAVZA$ is within the range $ID \pm A(I)$. The linear regression (Fig. 7 blue lines) of the mean GOES-minus-MODIS LST bias with respect to $CAVZA$ constitutes the nadir-normalized VZA correction model,

$$\Delta T = a_1 CAVZA + a_0, \quad (11)$$

where a_1 and a_0 are regression coefficients. The regression is tuned such that, for perfect nadir matching (i.e., $CAVZA = 1$ or $\Delta VZA = 0$), the ΔT adjustment is zero. This modification is made in order to prevent GOES-13 and Aqua-MODIS calibration differences (less than 0.35 K on average) from contributing false biases to the $CAVZA$ dependency. That is, the bias difference between GOES and MODIS should only be a function of increasing VZA difference, and therefore must not be influenced by pre-existing calibration bias, which does not contribute to $CAVZA$ dependency. The ΔT adjustment applied to satellite-derived skin temperature at $CVZA$, i.e., $T_{s,sat}(CVZA_{sat})$, yields nadir-normalized satellite-derived skin temperature, i.e., $T_{s,sat}(CVZA_{nadir})$, as follows:

$$T_{s,sat}(CVZA_{nadir}) = T_{s,sat}(CVZA_{sat}) - \Delta T(CVZA_{sat}) \quad (12)$$



Note that although the model is designed for application with *CAVZA*, it can be referred to as a VZA adjustment or correction for simplicity.

Further criteria beyond *CAVZA* stratification were required for including matched GOES-13 and MODIS pairs in the analysis. Both the GOES-13 and MODIS T_s averages for each $1.0^\circ \times 1.0^\circ$ grid cell must be based on, at least, 125 pixels. For the mean bias at a given *CAVZA* interval to qualify for use in the model, that interval regression must consist of at least 75 individual matched grid cells with $SDD < 2.5$ K. The sample limits of 125 and 75 were found to be an acceptable balance between sample-per-interval allowance and model stability. That is, these criteria are necessary to minimize uncertainties in the model while maximizing the *CAVZA* dynamic range.

A systematic relationship between increasing viewing angle and negative GOES- minus-MODIS daytime LST bias is evident for April, July, and October (Figs. 7b-7d). During the day, as the GOES VZA increases (*CAVZA* decreases), the GOES-retrieved LST decreases relative to the nadir MODIS-retrieved LST. During the day in January (Fig. 7a) and at night for all months (Fig. 8), the viewing angle dependency of LST is virtually non-existent. Nighttime anisotropy effects, induced either by differential cooling (Minnis and Khaiyer, 2000) or varying emissivity contributions caused by different fractional amounts of vegetation in the sensor FOV (Vinnikov et al., 2012), were not detected in this empirical approach. The result in Fig. 8, however, is not unexpected. Pinheiro et al. (2006) and Guillevic et al. (2013) found nighttime LST to be independent of viewing considerations, and conclude along with Minnis and Khaiyer (2000) that the primary cause of anisotropy is shadowing, with lesser contributions from evaporative cooling and surface air temperature gradients. The lack of a daytime VZA dependency during January (Fig. 7a) is surprising given that the average SZAs are larger in the Northern Hemisphere during January. It is evident, however, that the daytime VZA dependency is greatest when the sun is highest in North America. Whether this seasonal dependency is representative of variations around the globe will require much additional analysis beyond the scope of this paper.

The anisotropy correction for the SatCORPS SST employs a wind and viewing angle-dependent sea surface emissivity model based on theoretical calculations using a 5-knot wind speed (Jin et al. 2006). The results in Fig. 9 demonstrate that the model is quite effective at minimizing the dependence of SST on VZA. The bias is essentially zero across the VZA range and is accompanied small SDD. Therefore, as with nighttime land cases, an additional nadir-normalization model appears to be unnecessary for ocean scenes.

The dependence of the LST can also be expressed in terms of the variation of surface emissivity with VZA. This is illustrated in Fig. 10, which plots the ratios of the mean surface-leaving-radiances (L) from GOES-13 (GE) to those from the matched near-nadir Aqua-MODIS, along with linear regression fits of the data as a function of the *CAVZA*. In this case, the surface emissivity would be characterized as

$$\varepsilon_s(CAVZA) = \varepsilon_s(b_1CAVZA + b_0) \quad (13)$$

The slopes, b_1 , and offsets, b_0 , are shown in Fig. 10 for each month. As expected from Fig. 7, the slope is negligible for January (Fig. 10a) and is greatest for April (Fig. 10b). The apparent nonlinearity for $CAVZA < 0.6$ during April and July (Fig. 10c) may be an artifact of the reduced sampling at the higher VZAs (see Fig. 7).

5.2 Validation with independent MODIS LST, MYD11

The JAO 2013 GOES-13 LST values are compared with the independent MYD11 product to determine if the VZA parameterization improves the consistency of the two products. The GOES-13 10.8- μm channel was first cross-calibrated as in Minnis et al. (2002) against its Aqua-MODIS counterpart, channel 31, to minimize any calibration differences. Spectral differences were taken into account as in Scarino et al. (2016), but are based on Infrared Atmospheric Sounding Interferometer spectral measurements. For each Aqua overpass, the MYD11 pixel LST values are averaged on the $1^\circ \times 1^\circ$ GOES-East domain



and matched to within 15 minutes of the GOES-13 hourly scans, provided there are at least 150 valid MODIS and GOES-13 pixels per grid cell. To eliminate any differences due to surface emissivity discrepancies, the GOES-13 LST was retrieved using the MYD11 11.0- μm emissivity values. To effect the comparisons, the GOES-13 LST values were normalized to the MYD11 view, i.e., $CVZA_{myd}$, to yield $T_{s,sat}(CVZA_{myd})$ as follows:

$$5 \quad T_{s,sat}(CVZA_{myd}) = T_{s,sat}(CVZA_{sat}) - \left[\Delta T(CVZA_{sat}) - \Delta T(CVZA_{myd}) \right] \quad (14)$$

The appropriate model in Fig. 7 is used to compute DT in Eq (14) for each of the 4 months of matched data.

Figure 11 shows histograms of the differences between the GOES-13 and MYD11 LSTs without (Fig. 11a) and with (Fig. 11b) the daytime VZA corrections. Without correction, the GOES LSTs tend to be slightly greater than their MYD11 counterparts, especially during the daytime. The SDD is less than 1.9 K for all scenes, and the day and night GOES biases are 0.42 K and 0.11 K, respectively, resulting in a combined (both day and night) 0.28-K bias. After applying Eq (14) using the daytime corrections from the appropriate months, the daytime SDD and bias drop to 1.76 K and 0.08 K, respectively. The nocturnal bias drops to almost -0.2 K, while its SDD increases slightly. Applying the daytime corrections at night does not improve the comparisons, although the mean combined bias of -0.04 K is somewhat closer to zero. If the daytime correction is used during day only, the combined bias and SDD are 0.09 K and 1.49 K, respectively. It is clear that normalizing the VZAs of the two retrievals yields better agreement during the day, but it appears that no VZA correction is needed at night for the MYD11 data, as in accordance with the Fig. 8 results.

Similar results (not shown) were found for the GOES-13 LST values retrieved using GFS instead of MERRA. Unlike the SST comparisons (Figs. 4 and 5), the GFS-derived GOES LST bias and SDD values are comparable to those based on the MERRA profiles. Without applying the VZA corrections, the nocturnal and daytime biases for GOES/GFS retrievals relative to MYD11 are 0.14 ± 1.12 K and 0.54 ± 2.07 K, respectively, which are not significantly worse than the corresponding MERRA values. After applying the VZA adjustment, the night and day biases are -0.15 ± 1.18 K and 0.20 ± 1.93 K, respectively. Although the GFS results over land, compared to ocean, are much closer to those from MERRA, the MERRA-based results are slightly more accurate, relative to MYD11, than their GFS counterparts.

5.3 GOES-East/West LST comparison

To further test the efficacy of the VZA corrections, differences between the hourly GE and GOES-West (GW) LST retrievals from July 2013 were computed before and after applying the daytime July VZA adjustment. Prior to differencing, the 15-minute discrepancy in the image retrieval at the 3-hourly synoptic times (00, 03, ..., 21 UTC) was mitigated by adjusting the GE LST, which is based on images beginning 15 minutes before the UTC hour, to that UTC hour when the GW image scan began. This approach accounts for the specific GE and GW scanline time discrepancies. The GE data were linearly interpolated to the GW time using the nearest surrounding synoptic hours. When those surrounding hours crossed the sunrise terminator, no correction was applied because of the day-night discontinuity in LST that occurs shortly after sunrise. Data taken near the terminator (solar zenith angle between 80° and 100°) were not used. The image times at the non-synoptic hours are nearly identical, so no temporal normalization was required. To minimize calibration differences, the average nocturnal LST difference, 0.08 K, between GOES-13 and 15 within 0.5° longitude of 105°W , which is bisector of the two views, was computed and added to all GOES-15 (GW) values.

Figure 12 plots the VZAs for GW (Fig. 12a), GE (Fig. 12b), and the GE – GW VZA differences (Fig. 12c). Although the differences are generally less than $\pm 30^\circ$, the largest VZAs are up to 70° or more, so $CVZA$ can be as much as 0.35. Figure 7c would suggest large LST differences for pairs matched at the higher VZAs in this domain. All the retrieved values of normalized LST for both satellites were adjusted to nadir using the equation in Fig. 7c to account for the VZA dependence.



The mean regional differences, i.e., $DT_s = \text{LST}(\text{GE}) - \text{LST}(\text{GW})$, are shown in Fig. 13 for the matched July 2013 data. During daytime, DT_s for the unadjusted values (Fig. 13a) is mostly positive east of 105°W and negative to the west. Notable exceptions include the positive values in the west corresponding the highest mountain ranges in Colorado, Utah, Mexico, Washington, Wyoming, Idaho, and New Mexico. After adjusting to nadir (Fig. 13b), the same patterns remain, but the DEW values are closer to zero except for those in the high mountain areas, which are enhanced with the adjustment. Also, the corrected differences for some of the regions at extreme VZAs in the far northeast remain relatively large, perhaps because the viewing dependence increases with VZA with a greater slope for $VZA > 60^\circ$ as suggested by Fig. 10c. At night, the unadjusted differences (Fig. 13c) are relatively small, $|DT_s| < 2$, in most regions. The positive differences are no longer evident over the high mountains. Applying the daytime VZA correction further reduces $|DT_s|$ to values less than 1.0 K in nearly all cases (Fig. 10d).

Table 1 summarizes the GE – GW results. Over the eastern and western halves of the domain, $|DT_s|$ drops by 0.97 K and 0.55 K, respectively, during the day with the application of the VZA adjustment. The mean regional differences are much smaller than before correction, especially for the western region where the difference is near zero. Similarly at night, the corresponding regional differences decrease by comparable amounts and are much closer to zero than without the corrections. Furthermore, the mean absolute biases for both day and night, which are determined by the east – west sample-weighted region differences (not shown), are much closer after correction – reduced by a factor of two or more. In contrast to the findings in the previous sections, there appears to be a dependence of T_s on VZA over land at night, at least, for the VZAs seen here, which are mostly greater than 40° . The reasons for the discrepancy at night are not immediately evident and warrant additional investigation in future studies. Overall, the mean bias for the entire domain after correction over all non-terminator hours is 0.59 K.

Although it significantly reduces the GE – GW differences, the VZA correction does not eliminate all of the disagreement between the two satellite retrievals. This is especially evident over the mountains. Also, although sign difference between the means over the eastern and western domains essentially disappears for both day and night with the correction, the remaining east-west difference suggests other factors aside from VZA affect the observed temperatures. It is likely that the solar azimuthal dependence seen in earlier studies (e.g., Minnis et al. 2004, Vinnikov et al. 2012) is not balanced out for the configurations seen here. The azimuthal dependence includes effects from both the relative solar azimuth angle and the azimuthal orientation of the terrain and vegetation. Moreover, the heating/cooling rates probably differ between the eastern and western domains because of humidity and altitude differences. Downwelling longwave radiation might play a greater role in the diurnal cycle of T_s in the eastern domain, perhaps diminishing the solar-induced anisotropy. Although the azimuthal dependencies are outside the purview of this paper, it is instructive to further explore how the differences change over the course of the day and how much the VZA correction diminishes the differences in more detail.

To that end, the differences were averaged for each UTC and are plotted in Fig. 14 as lines connecting the means at each hour. Over the western domain (red line), the uncorrected DT_s (Fig. 14a) gradually approaches zero at 09 UTC from ~ -1 K after 03 UTC, when the sun has set over the entire domain. At 12 UTC, it rises rapidly to a peak of 2.5 K near 16 UTC and drops precipitously after 17 UTC to -3 K at 22 UTC before increasing to 03 UTC. In the east (blue line), DT_s drops slowly toward zero after 01 UTC, but only reaches 0.4 K at 06 UTC before increasing again. It only increases significantly after 12 UTC, maximizing at 3.5 K (17 UTC) before decreasing to 1.3 K at 21 UTC, when it levels off. The relative behavior is the same for the corrected values (Fig. 13b), but the two curves are nearly identical between 03 and 17 UTC, being much closer to zero overall than without the VZA correction. After 17 UTC, the curves diverge with the western data changing more rapidly than their eastern counterparts suggesting different cooling rates. The bias for the entire domain (black line) shows definitively that the afternoon points are mainly responsible the overall positive bias in Table 1.



Even with different cooling rates, it is expected that DT_s would approach zero after correction for VZA effects as the surface air and skin temperature equilibrate. Instead of going to zero after 03 UTC, DT_s drops to roughly -0.3 K for the entire domain by 06 UTC and then rises to +0.5 K at 09 UTC, remaining flat until 12 UTC. This odd behavior is likely an artifact of the sun-satellite configuration, which causes a change in the infrared channel calibrations at satellite midnight and for 3-4 hours afterward. Yu et al. (2013) found that the GOES-11 and GOES-12 10.7- μm (channel 4) brightness temperatures were biased by -0.5 K relative to their daytime calibrations for 3-4 hours after satellite midnight, even after an operational correction for the midnight effect had been applied. A smaller bias was evident for a couple of hours prior to midnight. This residual bias could explain the unexpected variation in DT_s seen between 03 and 12 UTC, if GOES-13 and 15 suffer from a similar UTC bias. Assuming then that the calibration biases are -0.15 K and -0.30 K two hours before and for four hours after midnight, respectively, for GE and -0.25 K and -0.5 K for GW, then DT_s would almost follow the black curve in Fig. 14b exactly (assuming that $DT_s = 0$ in a perfectly calibrated system). By 06 UTC, DT_s would reach -0.30 K because only GE is influenced by the midnight effect. By 07 UTC, the smaller GW pre-midnight bias would partially offset the GE bias causing DT_s to rise until 09 UTC, when only GW is affected. After 12 UTC, the daylight in the eastern half of the domain would overwhelm any remaining bias.

The results here only represent one domain during one month. The $CDVZA$ functions in Fig. 7, the midnight calibrations, and the viewing and illumination angles vary with time of year. It is clear that much more comprehensive study would be needed to fully assess the VZA component of the angular dependence of the retrieved T_s values.

5.4 Validation with ground stations

The ground sites used for further validation consist of the ARM SGP and seven SURFRAD locations: Bondville, IL (BON), Desert Rock, NV (DRA), Fort Peck, MT (FPK), Goodwin Creek, MS (GWN), The Pennsylvania State University (PSU), Sioux Falls, SD (SXF), and Table Mountain, CO (TBL). To obtain estimates of the LST bias and SDD relative to ground site measurements, all 3x3-pixel arrays centered on each site, having confidently clear LST values, were selected from the GOES-13, GOES-15, and NOAA-18 AVHRR retrievals. Averages and standard deviations were computed for each array. Any array with a standard deviation greater than the 99th percentile of standard deviations for each site was eliminated to minimize the inclusion of any residual cloudiness in the arrays. After screening, the LST of the central pixel in each array was used for comparison with the SURFRAD station measurements, while the array mean LSTs are compared with the SGP data. It was determined that, in general, the central pixel yielded better comparisons than the array means owing to terrain heterogeneity. For relatively homogenous regions such as the SGP and SXF, however, either value could be used.

Figure 15 shows the scatterplots of LST retrieved from the ARM SGP IRT and from matched GOES and AVHRR data. The IRT is a down-looking narrow-field-of-view instrument, so it is considered to have a nadir view for this comparison. The points (Fig. 15a) tend to parallel the line of agreement, but are mostly above it. The IRT values are 1.10-K greater than their satellite counterparts. The SDD is nearly 2.0 K. If the daytime VZA corrections are applied to all of the data, the points are scattered about the line of agreement and the average difference is 0.02 K with SDD = 1.78 K. If comparing the central pixel rather than the 3x3 array average, the average difference is then -0.03 K with SDD = 1.68 K (not shown). With either scenario, the agreement improves for both daytime and nighttime points suggesting that the VZA dependency discussed in the previous section is valid for night also. This use of a daytime-based model for all hours may seem unattested, but given the conflicting results regarding the existence of nighttime VZA dependency, only the daytime model is available for assessing improvement at night. Overall, the results support its application to nighttime data.

This improvement for both halves of the diurnal cycle is easier to see in Fig. 16, which plots histograms of the differences, SatCORPS – IRT, before (Fig. 16a) and after (Fig. 16b) VZA correction. The daytime bias approaches zero, moving from -1.46



K to -0.30 K, while the nocturnal bias increases from -0.78 K to 0.30 K. The histograms narrow as SDD improves for both time periods. If only the GOES data are considered, the corrected data yield 0.03 ± 2.09 K and 0.28 ± 1.05 K for day and night, respectively. This suggests that AVHRR retrievals have slightly larger uncertainties during the day than the GOES retrievals. The same data were analyzed using the GFS atmospheric profiles and yielded smaller biases, -1.16 , -0.63 , and -0.86 K, for day, night, and all times, respectively, for no VZA correction (not shown). With the correction, the day and night biases of 0.07 K and 0.55 K, respectively, which combine to yield an overestimate of 0.34 ± 1.55 K. This bias is slightly larger than the MERRA-based retrievals, but the SDD is reduced by 13%. Thus, the overall accuracy is similar for the two vertical profile sources for this location.

The SURFRAD down-looking pyrometers, used for estimating T_s with Eq (2), are hemispherical sensors receiving radiation from all directions. Thus, the equivalent VZA for comparison is 53° , which corresponds to the diffusivity factor of 1.66. Equation (14) is used to effect the VZA corrections of the satellite data, except that $\cos(53^\circ)$ replaces $CVZA_{myd}$ in all of the appropriate terms. Because the viewing perspective of the SURFRAD sites from GE ranges from $\sim 43^\circ$ – 63° , the VZA difference is typically $< 10^\circ$, and as such most of the corrections will be relatively small. However, AVHRR views a given site over a wider range of VZAs, resulting in larger corrections for some overpasses.

Figure 17 shows the matched satellite and SURFRAD LSTs at Desert Rock, NV without (Fig. 17a) and with (Fig. 17b) the VZA adjustments applied. The change after applying the adjustments is negligible, as expected. During spring and winter, SatCORPS underestimates T_s from the surface, while it tends to match well during the summer and autumn months. Overall, the bias is close to -1.0 K for this site, which is located in a valley surrounded by low mountains that rise more 300 m from the valley floor. The GOES and AVHRR pixels could include some portion of the surrounding terrain given that the mountains are within 2.5 – 2.7 km from the site. The mountains could induce a small difference between satellite and surface-site temperatures. The LST differences over Sioux Falls, SD are plotted in Fig. 18, with two different colors depicting day (red) and night (blue) points. Without the VZA correction (Fig. 18a), the bias is slightly negative, but becomes slightly positive after correcting for the VZA (Fig. 18b). In both cases, the SDD is 1.86 K. The increase in T_s after correction brings the hotter daytime points in agreement, but overcorrects the colder points. The nighttime data are fairly well aligned in both cases. For this reference, there is minimal elevation change within 10 km of the site.

Table 2 gives the mean bias and SDD for all satellites together (bottom) and for the GOES retrievals alone (top) for each SURFRAD site using MERRA as the SatCORPS input. The averages of the surface emissivities used at each site are also given. Bias and SDD results are shaded to show where the VZA correction yielded improved (green) or degraded (red) results by an absolute change of more 0.05 K or greater. Smaller differences are considered negligible. Brighter shades indicate an absolute adjustment of 0.10 K or greater. The absolute biases for the combined day-night data are all less 1.0 K, except for TBL. Removing the AVHRR data from the comparisons (top) worsens the combined biases for SXF. However, most of the biases are smaller for the GOES-only results than for the combined satellites. For VZA-corrected GOES-only results, the ranges in SDDs are 1.21–2.10 K, 1.23–2.15 K, and 1.06–1.66 K for the combined, daytime, and nighttime sets, respectively. Adding the AVHRR data yields the corresponding ranges in SDD: 1.30–2.09 K, 1.28–2.36K, and 1.07–1.78 K. In general, the uncorrected SDDs are larger than their corrected counterparts.

The biases in the results can be due to many factors including errors in the assumed surface emissivities, the atmospheric profiles, and the surface observations themselves. The representativeness of the site for the much larger area is also potentially a large source of bias. This issue, sometimes called the up-scaling problem (Li et al., 2014; Guillevic et al., 2012), is a concern for any ground-based satellite LST validation effort, but no attempt is made here to up-scale the ground station point observations to fully characterize the relatively large pixel area of the satellite product. The potential impact of the large scale is important to



mention, however. For example, Guillevic et al. (2012) found that, in areas of mixed trees and open grass or farmland, tree canopy temperatures rise less during the day and drop less at night than the surrounding bare soil (open areas). Because the surface radiometers are typically located in open areas, they could read systematically warmer or colder than the average upwelling radiation for the entire domain, which encompasses canopies and surface-exposed areas. This may, in part, explain the day-night switch in the sign of the bias over GWN and PSU – two sites with considerable mixtures of trees and open fields. Heidinger et al. (2013) found a similar day/night bias change for those two sites. Topography can also be responsible, in part, for the biases. PSU and DRA are both located in valleys around which the elevation changes by 300-m or more within the area represented by a single pixel. The large negative bias at TBL may be due, in part, to elevation change around the site. These and other error sources should be explored in detail in future analyses.

The VZA adjustment generally improves the nocturnal biases and about half of the daytime biases. To quantify the improvement, the results from all of the SURFRAD sites were combined to produce the histograms in Fig. 19. Compared to the differences for the uncorrected data (Fig. 19a), the corrected SatCORPS temperatures (Fig. 19b) represent a slight improvement, day and night, in both bias and SDD, but produce a 0.04-K increase in absolute bias when all data are combined. Overall, the VZA-corrected temperatures generate biases and SDDs of -0.51 K and 2.13 K for daytime, respectively, and -0.01 and 1.77 K at night. The 3% drop in SDD for the combined data represents an almost negligible improvement in the precision. As noted earlier, however, the GOES VZAs relative to these sites are near the diffusivity angle, and the change was expected to be small. Furthermore, for the AVHRR data, a full range of VZAs was used, so that, on average, the correction should also be small. The only location where the VZA corrections were significant was the ARM SGP site, where the data were corrected to a nadir view. That adjustment was quite significant, taking the bias much closer to zero.

The GOES analyses were also performed using the GFS profiles as input. The mean differences and SDDs between all surface measurements, including the SGP site, and SatCORPS retrievals using both MERRA and GFS input are summarized in Table 3. Overall, the GFS soundings yield slightly larger SDDs and a greater positive nocturnal bias, which produces a smaller combined bias than found using the MERRA data. Although the LST retrievals are similar for both GFS and MERRA, they differ significantly for SSTs (Fig. 6). Thus, use of the MERRA profiles for retrieving T_s with a single IR channel is preferable. The combined day and night MERRA-sourced biases and SDDs are comparable to those of Heidinger et al. (2013) despite different assumptions and input, and are smaller than those from the current operational GOES product (Sun et al., 2012). Additionally, with the exception of daytime BON SDD, the individual site day and night MERRA-sourced accuracy and precision values, as well as GFS-sourced values with the exception of SXF SDD (not shown), are within the GOES-R specifications of 2.5 K and 2.3 K, respectively (Yu et al., 2010).

Heidinger et al. (2013) also reported very small changes in LST as a function of VZA and concluded that they are not a major concern. The VZA corrections developed here improve the absolute bias and SDD in nearly all cases (Table 3). Although the corrections can increase the bias at night, they reduce the SDD and absolute bias in the combined results. The VZA correction, on average, reduces the absolute bias and SDD by 0.2 K and 4%, respectively, for the 8 surface sites. These small improvements, together with the better satellite-to-satellite normalization in Fig. 13, demonstrate that adjustment of LST for VZA dependencies will result in a more accurate and uniform product. The VZA dependency is probably not a concern for $VZA < 45^\circ$, as suggested by Wan and Li (1997). However, as greater VZAs are used, particularly for GEOs, the VZA correction should be considered. The effects of the illumination angles on the retrievals, however, should also be taken into account as they clearly have the greatest impact during the day, as indicated by Fig. 14. That aspect of the retrieval problem remains for future study.



6. Summary and Conclusions

Accurate assessment of global climate and improvement of climate models, as well as numerical weather forecasts, rely on consistent land and ocean T_s measurements, among others. Atmospheric flux calculations depend on the robustness of such surface variables, and NWP analyses are driven by reliable and frequent state variable updates over large spatial domains.

5 Despite key downsides, satellite data are ideal sources of T_s given their model-ready retrieval schedule and broad continuous areal coverage. Thermal-infrared-derived T_s relies on accurate cloud clearing, atmospheric adjustment, and viewing angle dependency correction. Therefore, validation of satellite T_s relative to known standards is of critical importance.

The SatCORPS provides a T_s product retrieved from GEO and AVHRR sources using the same single-channel algorithm. The benefit of the single-channel approach is that this method is more universally applicable to historic and future satellite
10 instruments compared to the split-window technique. Having GEO and AVHRR T_s values derived from the same algorithm reduces relative uncertainty and, hence, are better able supplement one another. Validation of SST retrieved from both satellites demonstrates consistent accuracy and precision results of less than 0.1 K and 0.6 K relative to NOAA OI SST, respectively, for atmospheric corrections based on MERRA profiles. If GFS temperature and humidity profiles are used to account for atmospheric attenuation, however, the accuracy and precision values for the GEO SST exceed 0.6 K and 1.0 K, respectively. The
15 larger negative bias and precision relative to the MERRA-based results suggests that the GFS atmosphere is drier than MERRA over the oceans, on average. This result is surprising in that satellite (Tian et al., 2013) and radiosonde (Kennedy et al., 2011) comparisons indicate that MERRA is too dry at altitudes below 500 hPa.

Daytime LST retrievals can be significantly influenced by satellite viewing geometry. As such, a seasonally dependent empirical model was developed using nadir single-channel MODIS and GOES-13 LST retrievals to account for this angular dependency.

20 The model, which is formulated either as a temperature difference or emissivity adjustment, can be used to normalize a satellite LST to any viewing zenith angle. A nighttime VZA dependency was not observed, further supporting the idea that sun/shade discrepancy is the dominant driver of LST anisotropy. A January daytime VZA dependency was also not found, perhaps indicating the chief importance of emissivity differences resulting from terrain and canopy-surface configurations that change with VZA.

25 Land surface temperatures retrieved from July 2013 matched GOES-East and GOES-West data over North America showed distinct VZA-dependent differences. Normalization of the daytime LSTs to the nadir view using the July daytime correction model reduced the absolute bias by a factor of two. The remaining daytime differences are due to solar illumination effects that are not considered here. Despite the absence of any VZA dependence in the matched nighttime GOES – MODIS data, the GE – GW average nocturnal absolute LST difference is ~0.9 K. Applying the daytime VZA correction reduces the mean absolute bias
30 to ~0.2 K. The conflicting results from the two different satellite analyses may be the result of diminished sampling at high VZAs in the matched MODIS-GOES dataset, as most of the GOES-East/West pairs have VZA > 45°. This discrepancy in nocturnal VZA dependence between the two results should be examined further along with the midnight calibration effect, which causes a temporary bias in GEO LST for part of the night period.

The SatCORPS retrievals from GOES-13 were compared to the Collection-5 Aqua-MODIS LST product, a well-validated
35 dataset. Normalization of the daytime GOES LSTs to the MODIS VZAs reduced the bias and SDD by roughly 0.3 K and 0.1 K, respectively, bringing the GOES data to within 0.1 ± 1.8 -K of the daytime MODIS product. Applying the daytime VZA normalization at night slightly worsened the comparison with MODIS, but when combined with the daytime data, it reduced the differences to nearly 0.0 ± 1.5 K. Use of the GFS profiles in place of their MERRA counterparts slightly degraded the precision to 1.6 K. Comparisons with LSTs from eight disparate ground stations provide further evidence of the validity of the SatCORPS
40 retrieval approach and the application of the VZA corrections, both for day and night. The VZA corrections increase the



accuracy by almost 50% and the precision by less than 10%, representing a net benefit. On average, MERRA-based atmospheric corrections seem to perform slightly better than GFS-based attenuation for LST retrievals compared to surface and other satellite LSTs. This finding, however, should not restrict use of GFS for LST retrievals, as the differences are rather small and not consistently better/worse in all scenarios. For SST validation, the MERRA atmosphere is clearly preferred.

5 This study has examined data from only one small part of the Earth over a limited range of angles for the VZA model development. It is not clear that a VZA-correction method developed for scenes over North America is applicable to other locations and the appropriate seasons. There remains some question about the behavior of the dependence at VZA > 45°, particularly at night. Many land areas are viewed at high VZAs by GEO imagers and, therefore, a more comprehensive characterization of the VZA dependence is warranted as satellite-to-satellite differences will produce climatological artifacts if the VZA dependence is not mitigated.

10 Further investigation is warranted for the SURFRAD validation approach, especially for the GWN, TBL, and PSU locations, and particularly in terms of the up-scaling problem. Disparity between pixel- and SURFRAD-observed surface conditions and topography-induced model sounding deficiencies are likely contributors to the surface-satellite differences. Beyond the outlier cases, however, the SatCORPS GEO and AVHRR T_s exhibit high accuracy and precision, with VZA-normalization affording reductions of 0.2 K and 0.1 K in daytime absolute LST bias and SDD, respectively. By incorporating these near-global NRT retrievals, the data assimilation and climate research communities will hopefully benefit from improved forecasts and better understanding of the global climate model.

Acknowledgments

This research was supported by the NASA Modeling, Analysis, and Prediction Program and the NOAA CDR Program. Computing was supported by the NASA High End Computing Program. The authors would like to thank Sarah Bedka and Doug Spangenberg for their generous assistance with MODIS skin temperature processing.

References

- Augustine, J. A., DeLuisi, J. J., and Long, C. N.: SURFRAD—A national surface radiation budget network for atmospheric research, *Bull. Am. Meteorol. Soc.*, 81, 2341–2357, doi:10.1175/1520-0477, 2000.
- 25 Bodas-Salcedo, A., Ringer, M., and Jones, A.: Evaluation of the surface radiation budget in the atmospheric component of the Hadley Centre Global Environmental Model (HadGEM1). *J. Climate*, 17, 4723–4748, 2008.
- Bosilovich, M., Radakovich, J., Silva, A.D., Todling, R., and Verter, F.: Skin temperature analysis and bias correction in a coupled land-atmosphere data assimilation system. *J. Meteorol. Soc. Jpn.*, 85A, 205–228, 2007.
- Chen, Y., Sun-Mack, P., Minnis, D. F., Young, W. L., and Smith, Jr., W. L.: Seasonal surface spectral emissivity derived from Terra MODIS data. *Proc. 13th AMS Conf. Satellite Oceanogr. and Meteorol.*, Norfolk, VA, Sept. 20–24, CD-ROM, P2.4, 2004.
- 30 Chen, Y., Minnis, P., Sun-Mack, R. F., Arduini, R., and Trepte, Q. Z.: Clear-sky and surface narrowband albedo datasets derived from MODIS data. *Proc. AMS 13th Conf. Atmos. Rad. and Cloud Phys.*, Portland, OR, June 27 – July 2, JP1.2., 2010.
- Coll, C. and Caselles, V.: A split-window algorithm for land surface temperature from advanced very high resolution radiometer data: Validation and algorithm comparison. *J. Geophys. Res.*, 102 (D14), 16697–16713, 1997.
- 35 Cuenca, J., and Sobrino, J.: Experimental measurements for studying angular and spectral variation of thermal infrared emissivity, *Appl. Opt.*, 43, 4598–4602, doi:10.1364/AO.43.004598, 2004.
- DaCamara, C. C.: The Land Surface Analysis SAF: One year of pre-operational activity. In



- Proc. 2006 EUMETSAT Meteorol Satellite Conf., Helsinki, Finland, 2006.
- Draper, C., Reichle, R., De Lannoy, G., and Scarino, B.: A dynamic approach to addressing observation-minus-forecast mean differences in a land surface skin temperature data assimilation system, *J. Hydrometeorol.*, 16, 449–464, 2013.
- Environmental Modeling Center, 2003: The GFS Atmospheric Model. NCEP Office Note 442, Global Climate and Weather
5 Modeling Branch, EMC, Camp Springs, Maryland.
- Garand, L.: Toward an integrated land-ocean surface skin temperature analysis from the variational assimilation of infrared radiances, *J. Appl. Meteorol.*, 42, 570–583, 2003.
- Göttsche, F. M., Olesen, F. S., and Bork-Unkelbach, A.: Validation of land surface temperature derived from MSG/SEVIRI with in-situ measurements at Gobabeb, Namibia, *Int. J. Remote Sens.*, 34, 3069–3083, 2013.
- 10 Goody, R., West, R., Chen, L., and Crisp, D.: The correlated-k method for radiation calculations in nonhomogeneous atmospheres, *J. Quant. Spectrosc. Radiat. Transfer*, 42, 539–550, 1989.
- Guillevic, P. C., Bork-Unkelbach, A., Göttsche, F. M., Hulley, G., Gastellu-Etchegorry, J.-P., Olesen, F. S., and Privette, J. L.: Directional viewing effects on satellite land surface temperature products over sparse vegetation canopies—A multisensor analysis, *IEEE Geo. Rem. Sens. Lett.*, 10 (6), 1464–1468, 2013.
- 15 Guillevic, P. C., Privette, J. L., Coudert, B., Palecki, M. A., Demarty, J., Ottlé, C., and Augustine, J. A.: Land surface temperature product validation using NOAA’s surface climate observation networks – Scaling methodology for the Visible Infrared Imager Radiometer Suite (VIIRS). *Rem. Sens. Env.*, 124, 282–298, 2012.
- Heidinger, A. K., Laszlo, I., Molling, C. C., and Tarpley, D.: Using SURFRAD to verify the NOAA single-channel land surface temperature algorithm, *J. Atmos. Ocean. Tech.*, 30, 2868–2884, 2013.
- 20 Jiménez-Muñoz, J. C., and Sobrino, J. A.: A single-channel algorithm for land-surface temperature retrieval from ASTER data, *IEEE Geosci. Remote Sens. Lett.*, 7, 176–179, 2010.
- Jiménez, C., Prigent, C., Catherinot, J., Rossow, W., and Liang, P. A.: Comparison of ISCCP land surface temperature with other satellite and in situ observations, *J. Geophys. Res.*, 117 (D8), doi:10.1029/2011JD017058, 2012.
- Jin, Z., T. P. Charlock, K. Rutledge, K. Stamnes, and Y. Wang: Analytical solution of radiative transfer in the coupled
25 atmosphere-ocean system with a rough surface. *Appl. Opt.*, 45, 7443–7455, 2006.
- Kabsch, E., Olesen, F. S., and Prata, F.: Initial results of the land surface temperature (LST) validation with the Evora, Portugal ground-truth station measurements, *Int. J. Remote Sens.*, 29, 5329–5345, 2008.
- Kennedy, A. D., Dong, X., Xi, B., Xie, S., Zhang, Y., and Chen, J.: A comparison of MERRA and NARR reanalyses with the DOE ARM SGP data. *J. Climate*, 24, 4541–4557, 2011.
- 30 Kerr, Y. H., Lagouarde, J. P., Nerry, F., and Ottlé, C.: Land surface temperature retrieval: Techniques and applications: Case of the AVHRR, in “Thermal Remote Sensing in Land Surface Processes”. Dale A. Quattrochi and Jeffrey C. Luvall, CRC Press 2004.
- Kratz, D. P.: The correlated k-distribution technique as applied to the AVHRR channels, *J. Quant. Spectrosc. Radiat. Transfer*, 53, 501–507, 1995.
- 35 Lagouarde, J. P., Kerr, Y. H., and Brunt, Y.: An experimental study of angular effect on surface temperature for various plant canopies and bare soils. *Agric. For. Meteorol.*, 77, 167–190, doi:10.1016/0168-1923(95)02260-5, 1995.
- Lazzara, M. A., J. M. Benson, R. J. Fox, D. J. Laitsch, J. P. Rueden, D. A. Santek, D. M. Wade, T. M. Whittaker, and J. T. Young: The Man computer Interactive Data Access System: 25 years of interactive processing. *Bull. Amer. Meteor. Soc.*, 80, 271–284.



- Li, Z.-L., Tang, B.-H., Wu, H., Ren, H., Yan, G., Wan, Z., Trigo, I. F., and Sobrino, J. A.: Satellite-derived land surface temperature: Current status and perspectives, *Remote Sens. Environ.*, 131, 14–37, 2013.
- Minnis, P. and Khaiyer, M. M.: Anisotropy of land surface skin temperature derived from satellite data, *J. Appl. Meteorol.*, 39, 1117–1129, 2000.
- 5 Minnis, P., Nguyen, L., Doelling, D.R., Young, D.F., Miller, W.F., Kratz, D.P.: Rapid calibration of operational and research meteorological satellite imagers, Part II: Comparison of infrared channels. *J. Atmos. Oceanic Technol.*, 19, 1250–1266, 2002.
- Minnis, P., Gambheer, A. V., and Doelling, D. R.: Azimuthal anisotropy of longwave and infrared window radiances from CERES TRMM and Terra data, *J. Geophys. Res.*, 109, D08202, doi:10.1029/2003JD004471, 2004.
- Minnis, P., Nguyen, L., Palikonda, R., Heck, P. W., Spangenberg, D. A., Doelling, D. R., Ayers, J. K., Smith, Jr., W. L., Khaiyer,
10 M. M., Trepte, Q. Z., Avey, L. A., Chang, F.-L., Yost, C. R., Chee, T. L., and Sun-Mack, S.: Near-real time cloud retrievals from operational and research meteorological satellites, *Proc. SPIE Europe Remote Sens. 2008*, Cardiff, Wales, UK, 15-18 September, 7107-2, 8 pp., 2008a.
- Minnis, P., Trepte, Q. Z., Sun-Mack, S., Chen, Y., Doelling, D. R., Young, D. F., Spangenberg, D. A., Miller, W. F., Wielicki, B. A., Brown, R. R., et al.: Cloud detection in nonpolar regions for CERES using TRMM VIRS and Terra and Aqua MODIS data,
15 *IEEE T. Geosci. Remote Sens.*, 2008, 3857–3884, 2008b.
- Minnis, P., Sun-Mack, S., Trepte, Q. Z., Chang, F.-L., Heck, P. W., Chen, Y., Yi, Y., Arduini, R. F., Ayers, J. K., Bedka, K., Bedka, S., Brown, R., Gibson, S., Heckert, E., Hong, G., Jin, Z., Palikonda, R., Smith, R., Smith, Jr., W. L., Spangenberg, D. A., Yang, P., Yost, C. R., and Xie, Y.: CERES Edition 3 cloud retrievals. *AMS 13th Conf. Atmos. Rad.*, Portland, OR, June 27 – July 2, 5.4, 2010.
- 20 Minnis, P., Sun-Mack, S., D. F. Young, D. F., Heck, P. W., Garber, D. P., Chen, Y., Spangenberg, D. A., Arduini, R. F., Trepte, Q. Z., Smith, Jr., W. L., Ayers, J. K., Gibson, S. C., Miller, W. F., Chakrapani, V., Takano, Y., Liou, K.-N., Xie, Y., and Yang, P.: CERES Edition-2 cloud property retrievals using TRMM VIRS and Terra and Aqua MODIS data, Part I: Algorithms, *IEEE T. Geosci. Remote Sens.*, 49, 4374–4400, 2011.
- Minnis, P., Bedka, K., Yost, C. R., Bedka, S. T., Trepte, Q., Scarino, B., Khlopenkov, K., and Khaiyer, M. M.: A consistent
25 long-term cloud and clear-sky radiation property dataset from the Advanced Very High Resolution Radiometer (AVHRR). *Climate Algorithm Theoretical Basis Document (C-ATBD)*, CDRP-ATBD-XXXX, NOAA CDR Program, 125 pp., in press, 2016.
- Morris, V. R.: *Infrared Thermometer (IRT) Handbook*, U.S. Department of Energy, Office of Science, Office of Biological and Environmental Research. ARM TR-015, 2006.
- 30 (Available at https://www.arm.gov/publications/tech_reports/handbooks/irt_handbook.pdf).
- Pinheiro, A. C. T., Privette, J. L., and Guillevic, P.: Modeling the observed angular anisotropy of land surface temperature in a Savanna, *IEEE T. Geosci. Remote Sens.*, 44, 1036–1047, 2006.
- Prata, A. J.: Surface temperatures derived from the advanced very high resolution radiometer and the along track scanning radiometer. 1. Theory, *J. Geophys. Res.*, 98, 16689–16702, 1993.
- 35 Prata, A. J.: Land surface temperature determination from satellites, *Adv. Space Res.*, 14, 15–26, 1994.
- Rasmussen, M. O., Pinheiro, A. C., Proud, S. R., and I. Sandholt, I.: Modeling angular dependences in land surface temperatures from the SEVIRI instrument onboard the geostationary Meteosat Second Generation satellites, *IEEE T. Geosci. Remote Sens.*, 48, 3123–3133, 2010.



- Rasmussen, M. O., Göttsche, F.-M., Olesen, F.-S., and Sandholt, I.: Directional effects on land surface temperature estimation from Meteosat Second Generation for savanna landscapes, *IEEE T. Geosci. Remote Sens.*, 49(11), 4458–4468, doi:10.1109/TGRS.2011.2144604, 2011.
- Reichle, R., Kumar, S. V., Mahanama, S. P. P., Koster, R. D., and Liu, Q.: Assimilation of satellite-derived skin temperature observations into land surface models, *J. Hydrometeor.*, 11, 1103–1122, 2010.
- Reynolds, R. W., Smith, T. M., Liu, C., Chelton, D. B., Casey, K. S., and Schlax, M. G.: Daily high-resolution-blended analyses for sea surface temperature, *J. Climate*, 20, 5473–5496, 2007.
- Rienecker, M. M., Suarez, M. J., Gelaro, R., Todling, R., Bacmeister, J., Liu, E., Bosilovich, M.G., Schubert, S. D., Takacs, L., Kim, G.-K., et al. MERRA: NASA’s Modern-Era Retrospective Analysis for Research and Applications, *J. Climate*, 24, 3624–3648, 2011.
- Rodell, M., Houser, P. R., Jambor, U., Gottschalk, J., Mitchell, K., Meng, C.-J., Arsenault, K., Cosgrove, B., Radakovich, J., Bosilovich, M., et al.: The global land data assimilation system. *Bull. Amer. Meteor. Soc.*, 85, 381–394, 2004.
- Scarino, B., Minnis, P., Palikonda, R., Reichle, R. H., Morstad, D., Yost, C., Shan, B., and Liu, Q.: Retrieving clear-sky surface skin temperature for numerical weather prediction applications from geostationary satellite data. *Remote Sens.*, 5, 342–366, 2013.
- Scarino, B. R., Doelling, D.R., Minnis, P., Gopalan, A., Chee, T., Bhatt, R., Lukashin, C., Haney, C.O. A Web-based Tool for Calculating Spectral Band Difference Adjustment Factors Derived from SCIAMACHY Hyper-spectral Data. *IEEE Trans. Geosci. Remote Sens.*, DOI: 10.1109/TGRS.2015.2502904, Jan., 2016.
- Snyder, W. and Wan, Z.: BRDF models to predict spectral reflectance and emissivity in the thermal infrared, *IEEE T. Geosci. Remote Sens.*, 36, 214–225, 1998.
- Sobrino, J.A., and Cuenca, J.: Angular variation of thermal infrared emissivity for some natural surfaces from experimental measurements, *Appl. Opt.*, 38(18), 3931–3936, doi:10.1364/AO.38.003931, 1999.
- Sobrino, J. A. and Romaguera, M.: Land surface temperature retrieval from MSG1-SEVIRI data, *Remote Sens. Environ.*, 92, pp. 247–254, 2004.
- Sobrino, J. A. Sòria, G., and Prata, A.J.: Surface temperature retrieval from Along Track Scanning Radiometer 2 data: Algorithms and validation, *J. Geophys. Res.*, 109, D11101, 2004.
- Sun, D. and Pinker, R.T.: Estimation of land surface temperature from a Geostationary Operational Environmental Satellite (GOES-8), *J. Geophys. Res.*, 108, doi:10.1029/2002JD002422, 2003.
- Sun, D., Fang, L., and Yu, Y.: GOES LST Algorithm Theoretical Basis Document, Version 3.0, NOAA NESDIS Center for Satellite Applications and Research, Camp Springs, MD, USA, 81 pp., 2012.
- Tian, B., Fetzer, E. J., Kahn, B. H., Teixeira, J., Manning, E., and Hearty, T.: Evaluating CMIP5 models using AIRS tropospheric air temperature and specific humidity climatology. *J. Geophys. Res.*, 118, 114–134, doi:10.1029/2012JD018607, 2013.
- Trepte, Q. Z., Minnis, P., Trepte, C. R., Sun-Mack, S., and Brown, R.: Improved cloud detection in CERES Edition 3 algorithm and comparison with the CALIPSO Vertical Feature Mask. *Proc. AMS 13th Conf. Atmos. Rad. and Cloud Phys.*, Portland, OR, June 27 – July 2, JP1.32, 2010.
- Trigo, I., Monteiro, I. T., Olesen, F., and Kabsch, E.: An assessment of remotely sensed land surface temperature, *J. Geophys. Res.*, 113, D17108, 2008.
- Tsuang, B., Chou, M., Zhang, Y., Roesch, A., and Yang, K.: Evaluations of land ocean skin temperatures of the ISCCP satellite retrievals and the NCEP and ERA reanalyses, *J. Climate*, 21, 308–330, 2008.



- Vinnikov, K. Y., Yu, Y., Goldberg, M. D., Tarpley, D., Ramanov, P., Istvan, L., and Chen, M.: Angular anisotropy of satellite observations of land surface temperature, *Geophys. Res. Lett.*, 39, L23802, doi:10.1029/2012GL054059, 2012.
- Wan, Z.: New refinements and validation of the MODIS land-surface temperature/emissivity products, *Remote Sens. Environ.*, 112, 59–74, 2008.
- 5 Wan, Z. and Dozier, J.: A generalized split-window algorithm for retrieving land-surface temperature measurement from space, *IEEE T. Geosci. Remote Sens.*, 34, 892–905, 1996.
- Wan, Z. and Li, Z.-L.: A physics-based algorithm for retrieving land-surface emissivity and temperature from EOS/MODIS data, *IEEE T. Geosci. Remote Sens.*, 35, 980–996, 1997.
- Wan, Z., Zhang, Y., Zhang, Q., and Li, Z.-L.: Quality assessment and validation of the MODIS global land surface temperature, *Int. J. Remote Sens.*, 25, 59–74, 2004.
- 10 Wan, Z., Zhang, Y., Zhang, Q., and Li, Z.: Validation of the land-surface temperature products retrieved from Terra Moderate Resolution Imaging Spectroradiometer data, *Remote Sens. Environ.*, 83, 163–180, 2008.
- Wilber, A. C., Kratz, D. P., and Gupta, S. K.: Surface emissivity maps for use in satellite retrievals of longwave radiation, NASA Tech. Report, NASA/TP-1999-209362, L-17861, 35 pp., 1999.
- 15 Yoo, H.: Evaluation of NCEP GFS cloud properties using satellite retrievals and ground-based measurements. Ph.D. Dissertation, Univ. Maryland, College Park, MD, 159 pp., doi:10.13016/M2W90T, 2012.
- Yu, Y., Tarpley, D., Privette, J. L., Flynn, L. E., Xu, H., Chen, M., Vinnikov, K. Y., Sun, D., and Tian, Y.: Validation of GOES-R satellite land surface temperature algorithm using SURFRAD ground measurements and statistical estimates of error properties, *IEEE T. Geosci. Remote Sens.*, 50(3), 704–713, doi:10.1109/TGRS.2011.2162338, 2012.
- 20 Yu, Y., Tarpley, D., Privette, J. L., Goldberg, M.D., Rama Varma Raja, M.K., Vinnikov, K. L., and Xu, H.: Developing algorithm for operational GOES-R land surface, temperature product. *IEEE T. Geosci. Remote Sens.*, 47, 936–951, 2009.
- Yu, Y., Tarpley, D., Xu, H., and Chen M.: GOES-R Advanced Baseline Imager (ABI) Algorithm Theoretical Basis Document for Land Surface Temperature, Version 2.5, NOAA NESDIS Center for Satellite Applications and Research, Camp Springs, MD, USA, 93 pp., 2012.
- 25 Yu, F., Wu, X., Rama Varma Raja, M. K., Li, Y., Wang, L., and Goldberg, M.: Diurnal and scan angle variations in the calibration of GOES imager infrared channels. *IEEE T. Geosci. Remote Sens.*, 51(1), 671–683, doi:10.1109/TGRS.2012.2197627, 2013.



Longitude	Day		Night		All	
	Before (K)	After (K)	Before (K)	After (K)	Before (K)	After (K)
< 105°W	2.38	1.41	1.18	0.29	2.07	1.10
> 105°W	-0.51	0.04	-0.55	0.00	-0.53	0.02
All	0.98	0.74	0.43	0.17	0.85	0.59

Table 1: July 2013 matched GOES-East minus GOES-West mean clear-sky surface skin temperature difference for regions east and west of 105°W. The sample-weighted average bias is shown in the bottom row.



Sites			BON		DRA		FPK		GWN		PSU		SXF		TBL	
			40.1°N, 88.4°W		36.6°N, 116.1°W		48.3°N, 105.1°W		34.3°N, 89.9°W		40.7°N, 77.9°W		43.7°N, 96.6°W		40.1°N, 105.2°W	
Mean surface emissivity			E11	ELW	E11	ELW	E11	ELW	E11	ELW	E11	ELW	E11	ELW	E11	ELW
			0.985	0.981	0.982	0.954	0.992	0.986	0.983	0.989	0.984	0.990	0.991	0.981	0.089	0.994
Data used and sampling			Temperature Differences (K)													
			Orig	Corr	Orig	Corr	Orig	Corr	Orig	Corr	Orig	Corr	Orig	Corr	Orig	Corr
GOES Only	All	Bias	0.67	0.51	-0.97	-0.88	-0.33	0.14	0.83	0.48	0.81	0.52	-0.04	0.21	-1.81	-1.71
		SDD	1.61	1.61	1.37	1.37	1.25	1.21	2.05	2.10	2.02	2.06	1.94	1.93	1.90	1.91
	Day	Bias	1.11	0.93	-1.36	-1.19	-0.25	0.24	-1.00	-1.37	-0.53	-0.84	0.10	0.39	-2.35	-2.25
		SDD	2.07	2.09	1.62	1.60	1.27	1.23	1.43	1.52	1.70	1.72	2.16	2.15	2.04	2.05
	Night	Bias	0.35	0.21	-0.74	-0.70	-0.53	-0.10	2.26	1.93	1.84	1.57	-0.25	-0.06	-1.37	-1.27
		SDD	1.07	1.06	1.15	1.18	1.18	1.13	1.08	1.11	1.60	1.63	1.56	1.54	1.65	1.66
GOES + AVHRR	All	Bias	0.99	0.80	-0.94	-0.96	-0.07	0.26	0.83	0.51	0.88	0.56	-0.07	0.06	-1.67	-1.65
		SDD	1.84	1.84	1.57	1.52	1.45	1.30	2.00	2.03	2.06	2.09	1.86	1.86	2.08	2.04
	Day	Bias	1.42	1.25	-1.00	-0.95	-0.13	0.29	-0.90	-1.22	-0.65	-0.97	-0.02	0.19	-2.36	-2.28
		SDD	2.35	2.36	1.97	1.79	1.40	1.28	1.46	1.55	1.76	1.79	2.11	2.11	2.23	2.18
	Night	Bias	0.69	0.48	-0.91	-0.97	0.04	0.21	2.23	1.91	1.90	1.56	-0.14	-0.09	-1.15	-1.17
		SDD	1.29	1.27	1.20	1.28	1.54	1.35	1.06	1.07	1.54	1.60	1.49	1.47	1.78	1.78

Table 2: Combined (bottom half only) mean bias and SDD values in Kelvins for each of the seven SURFRAD locations during day, night, and combined day and night conditions, before (Orig) and after (Corr) VZA correction. Top half: GOES-East and GOES-West. Bottom half: GOES-East, GOES-West, and AVHRR. Shades of green (red) indicate bias or SDD improvement (degradation) after applying the daytime VZA correction, for absolute changes greater than or equal to 0.05 K. Bright shades of green or red indicate an absolute change of at least 0.10 K. Coordinates and mean 11- μ m (E11) and broadband longwave (ELW) emissivities are also listed for each site.

5



MERRA	GOES		GOES Corrected		All		All Corrected	
	Bias	SDD	Bias	SDD	Bias	SDD	Bias	SDD
Day	-0.73	2.13	-0.41	2.07	-0.71	2.24	-0.47	2.15
Night	-0.14	1.69	0.09	1.59	-0.07	1.74	0.05	1.67
Combined	-0.42	1.94	-0.16	1.85	-0.37	2.01	-0.17	1.93
GFS	Bias	SDD	Bias	SDD	Bias	SDD	Bias	SDD
Day	-0.73	2.17	-0.43	2.08	-	-	-	-
Night	0.10	1.74	0.37	1.63	-	-	-	-
Combined	-0.30	2.00	-0.02	1.90	-	-	-	-

Table 3: Mean bias and SDD values based on results from the ARM and seven SURFRAD sites before and after VZA correction using only GOES data, and using both GOES and AVHRR results (All). SatCORPS retrievals based on MERRA (top) and GFS (bottom) input.

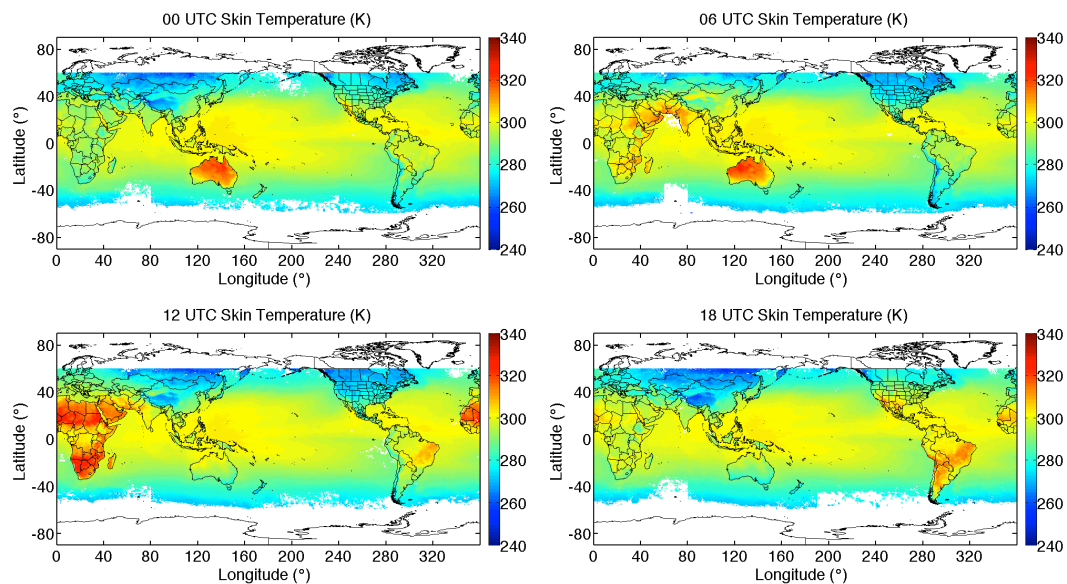


Figure 1: Mean merged, clear-sky surface skin temperature values from GOES-East, GOES-West, Meteosat-9, MTSAT-2, and INSAT-3D, October 2015.

5

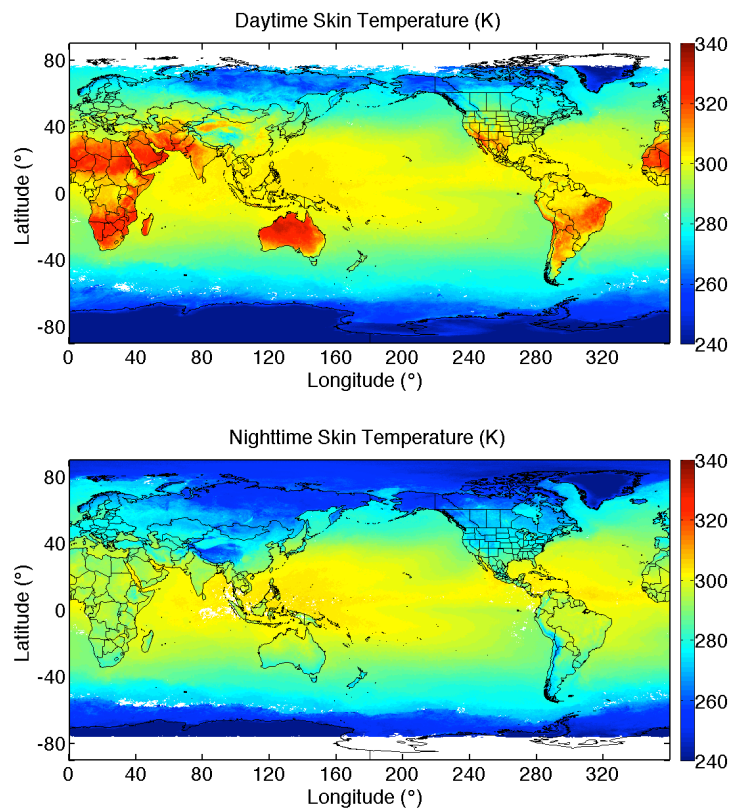


Figure 2: Average surface skin temperature from NOAA-18 AVHRR, October 2008.

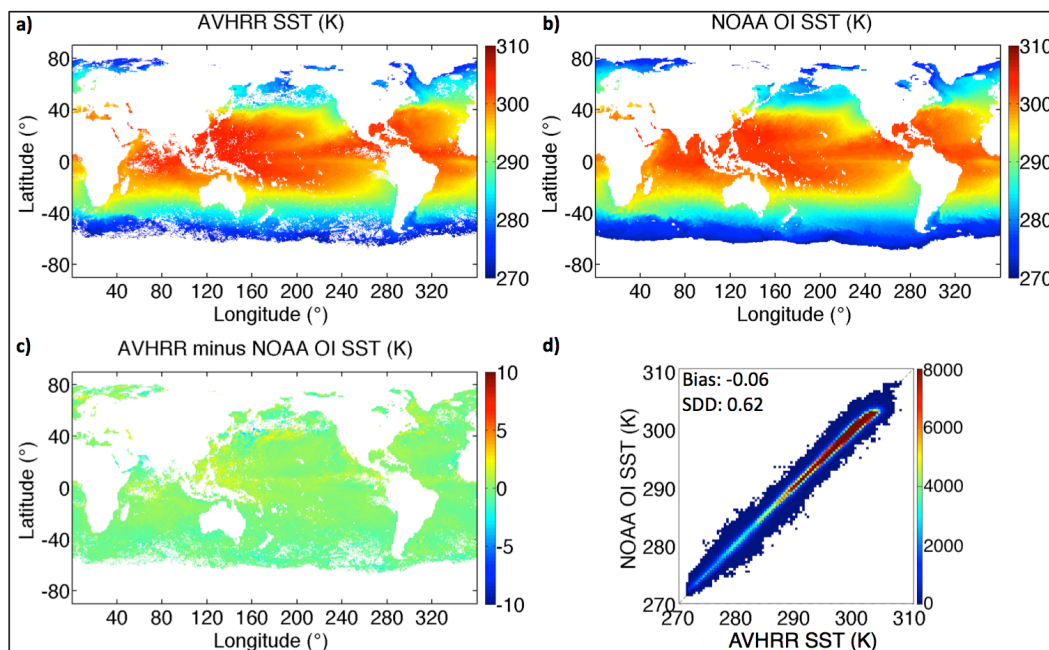


Figure 3: July 2008 a) AVHRR SST, b) NOAA OI SST, c) SST difference, and d) scatter density analysis of ~3 million daily matched grid cells.

5

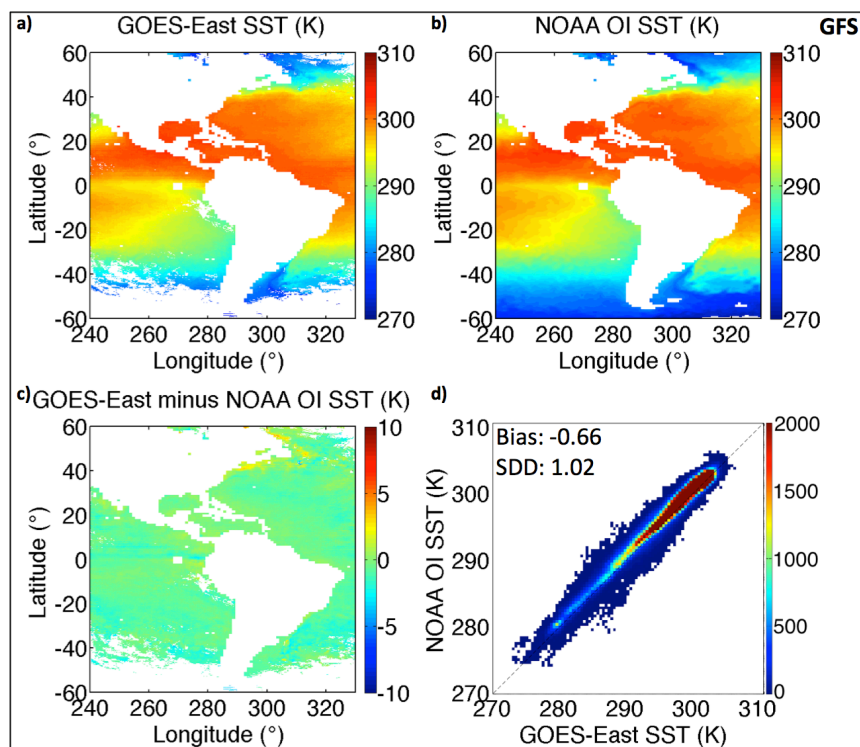


Figure 4: July 2013 a) GOES-13 SST derived, in part, from GFS-based atmospheric corrections, b) NOAA OI SST, c) SST difference, and d) scatter density analysis of ~1 million daily matched grid cells.

5

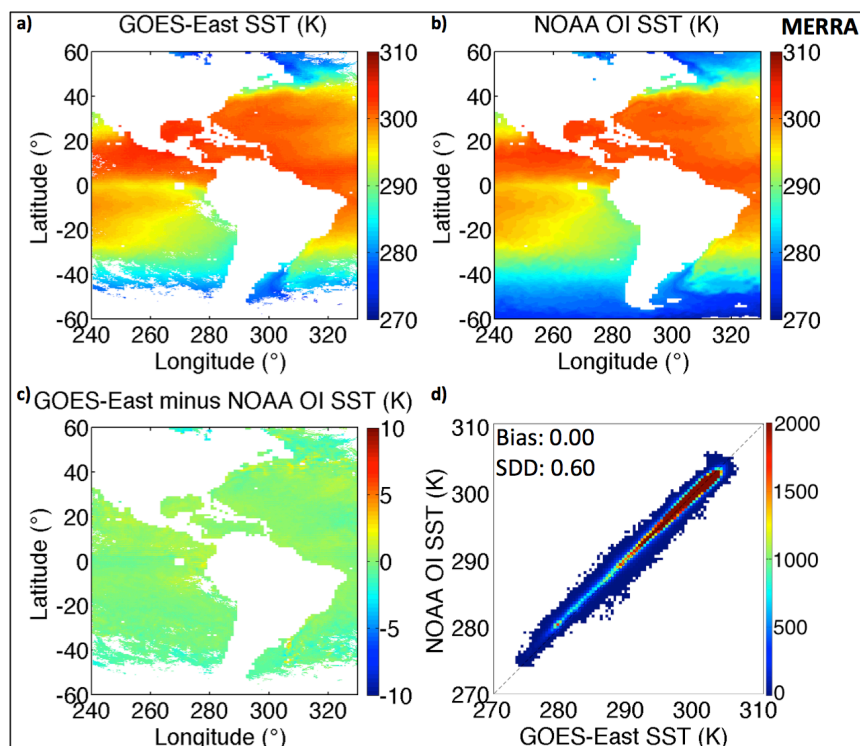


Figure 5: July 2013 a) GOES-13 SST derived, in part, from MERRA-based atmospheric corrections, b) NOAA OI SST, c) SST difference, and d) scatter density analysis of ~1 million daily matched grid cells.

5

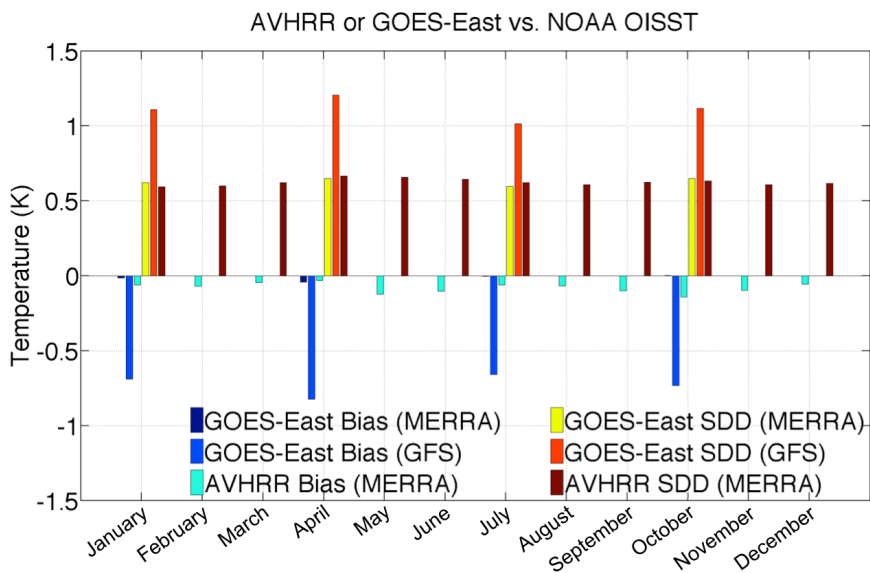


Figure 6: AVHRR (2008) and GOES-13 (2013) SST accuracy and precision relative to NOAA OI SST. For the GEO retrievals, the atmospheric correction is based on either GFS or MERRA reanalysis. Atmospheric corrections for AVHRR retrievals are strictly based on MERRA.

5

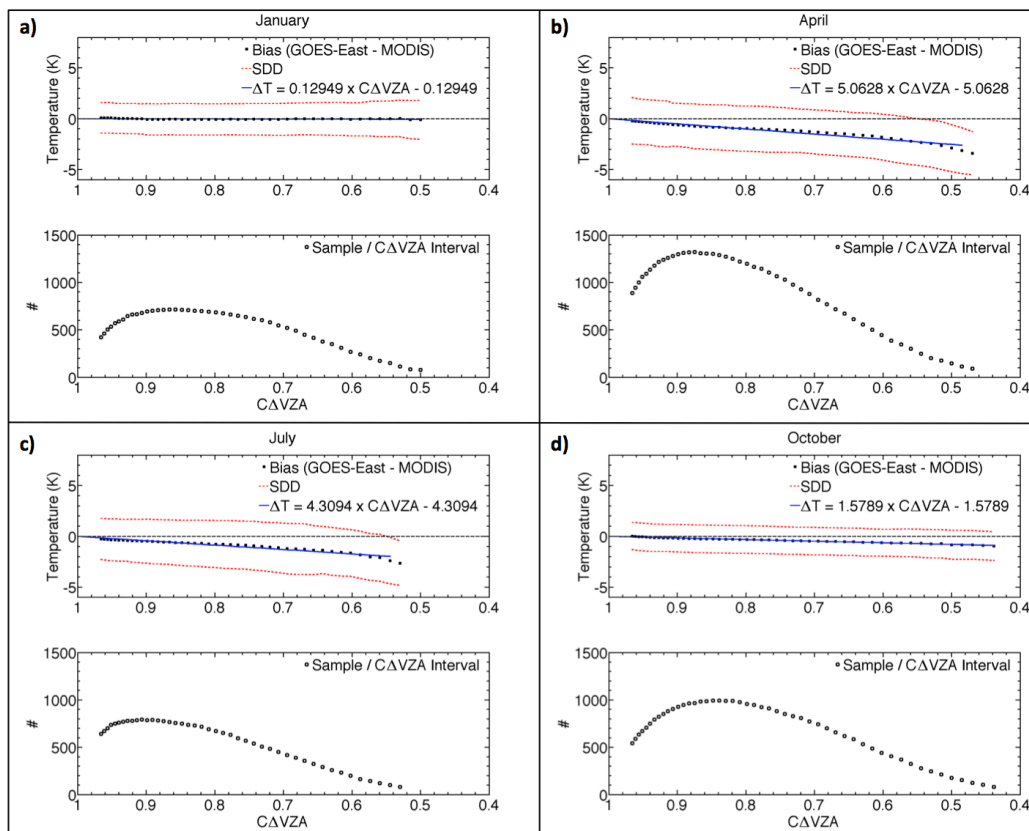


Figure 7: Daytime GOES-13-minus-MODIS LST bias (solid black dots) as a function of the cosine of the GOES-13-minus-MODIS VZA difference, for which MODIS retrievals are restricted to the nadir view, during a) January, b) April, c) July, and d) October 2013. The standard deviation of the difference (SDD) is indicated by the dotted red line. Black circles indicate the number of coincident GOES-13 and MODIS measurements at each $C\Delta VZA$ interval.

5

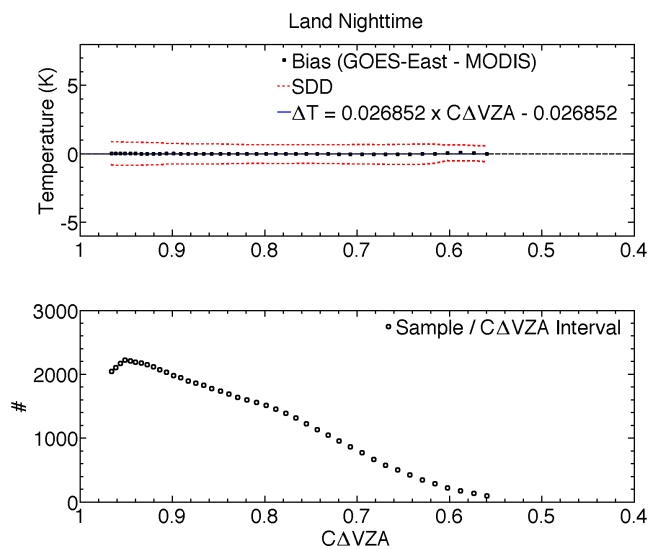


Figure 8: Same as Fig. 7, except for combined JAJO nighttime LST.

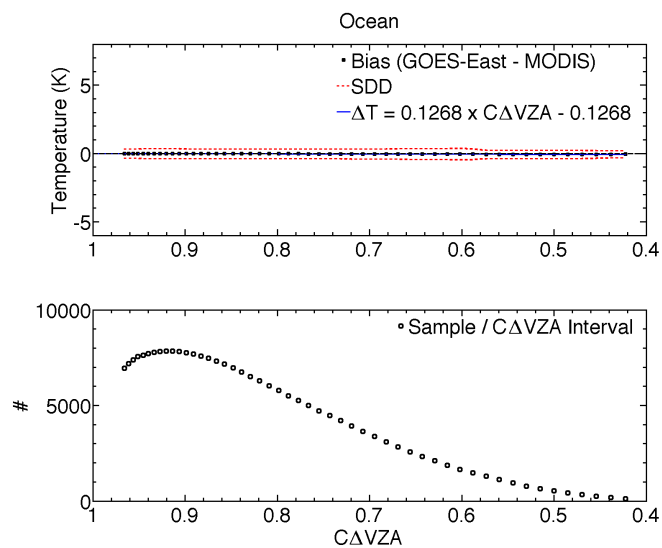


Figure 9: Same as Fig. 7, except for combined JAJO daytime and nighttime SST.

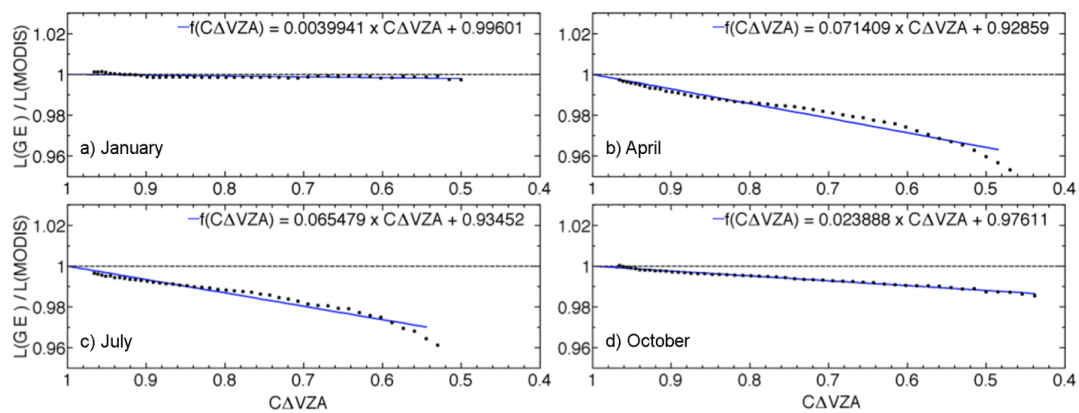


Figure 10: Same as Fig. 7, except for ratio of GOES-13 to Aqua-MODIS surface-leaving radiance. Sampling is the same as in Fig. 7.

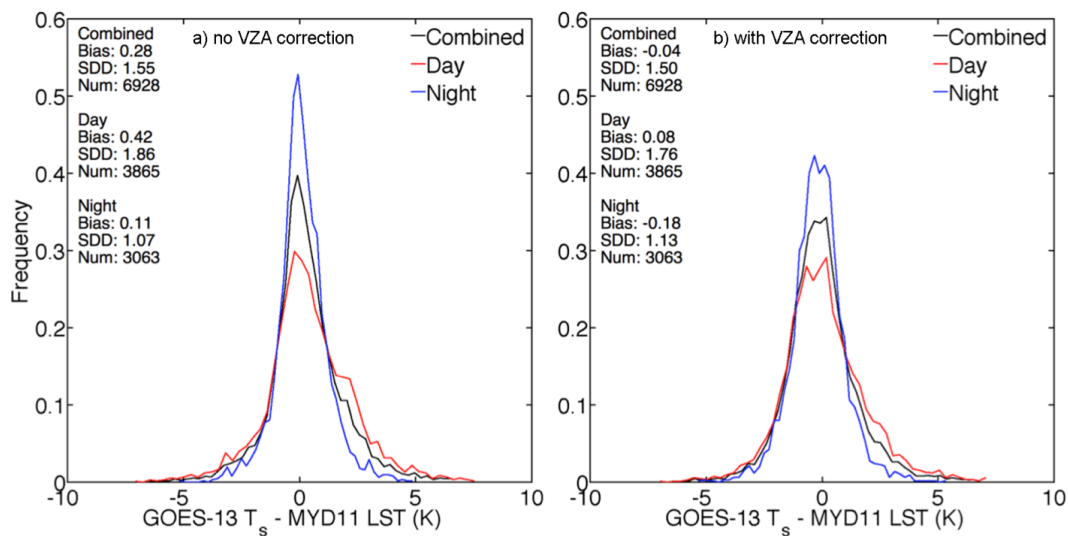


Figure 11: Probability distributions of LST differences from GOES-13 and the MYD11 Aqua-MODIS product for day, night, and all times (combined) (a) without and (b) with daytime viewing angle adjustments applied.

5

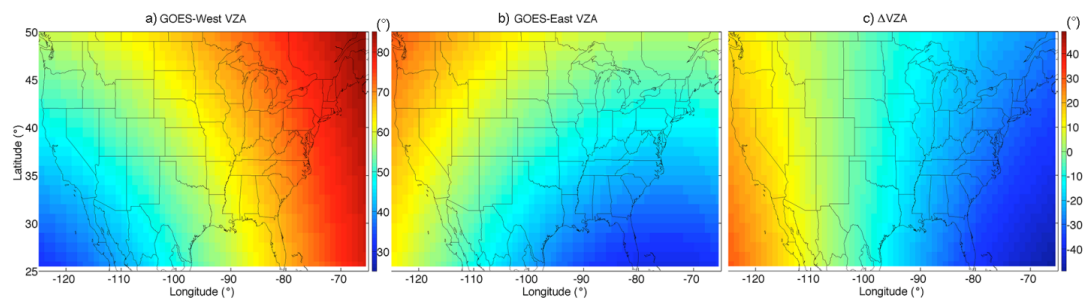


Figure 12: Viewing zenith angles for (a) GOES-West and (b) GOES-East, and (c) their differences over the matching domain.

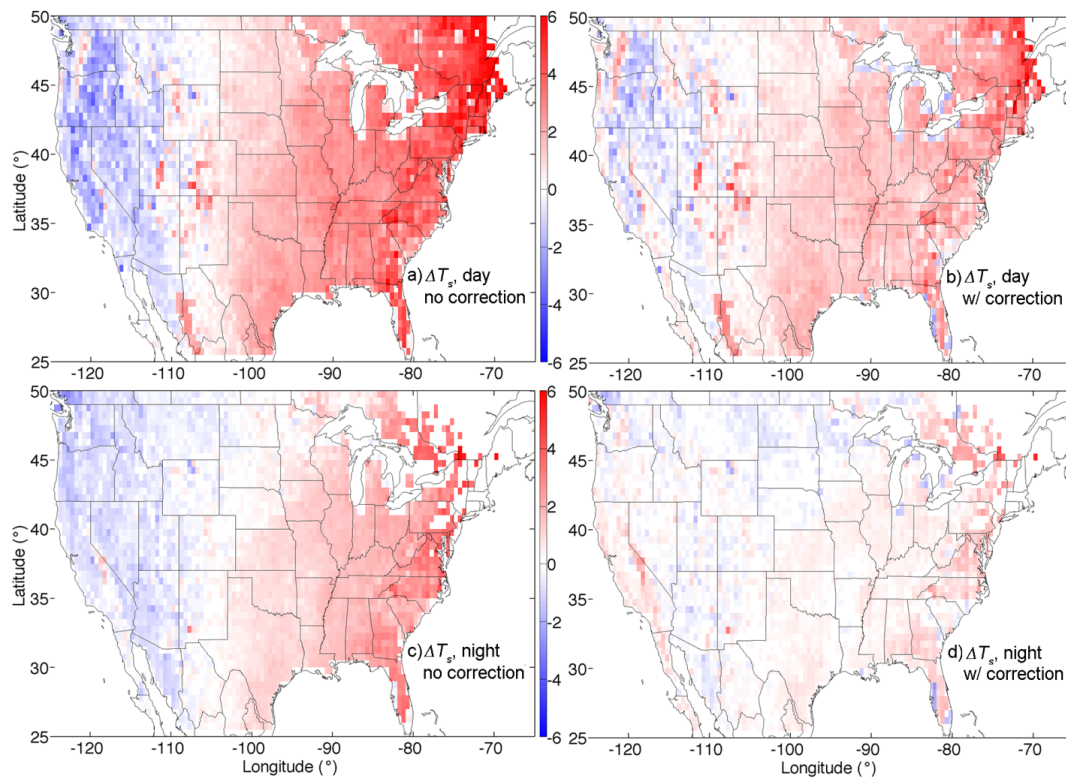


Figure 13: Mean regional GOES-East – GOES-West LST differences for July 2013. (a) Day and (c) night, no VZA adjustment. (b) Day and (d) night, with VZA adjustment.

5

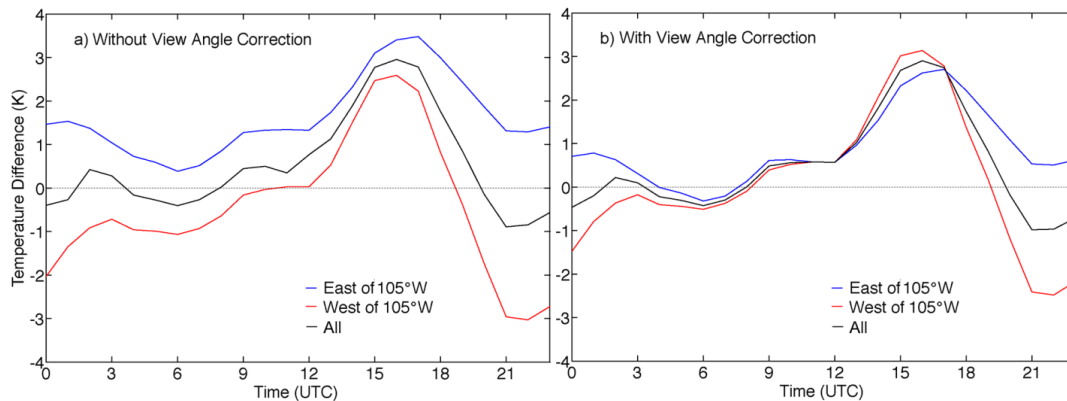


Figure 14: Mean hourly, regional GOES-East – GOES-West LST differences for July 2013.

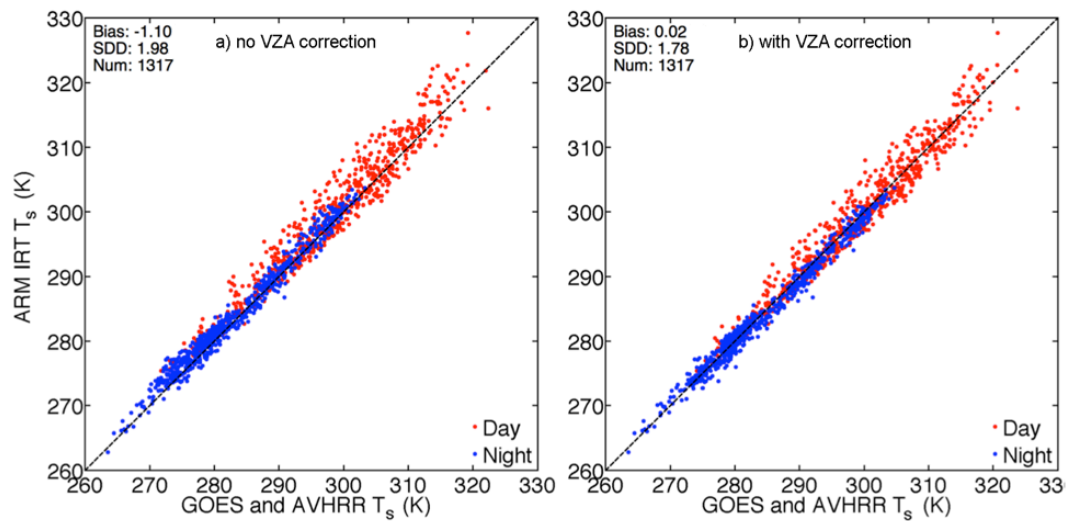


Figure 15: Scatterplots of clear-sky surface skin temperatures from JAO 2013 GOES-13 and 15 imagery, and from 2008 NOAA-18 AVHRR data, matched with ARM SGP IRT temperatures (a) without and (b) with VZA corrections.

5

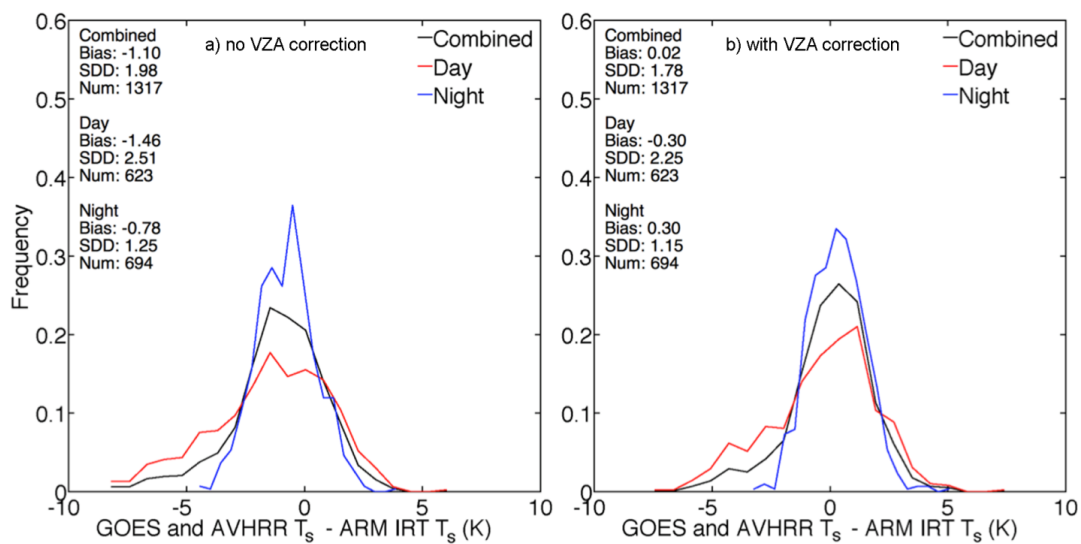


Figure 16: Histograms of LST differences between satellite (GOES-13, GOES-15, and AVHRR) and ARM IRT (a) without and (b) with VZA corrections.

5

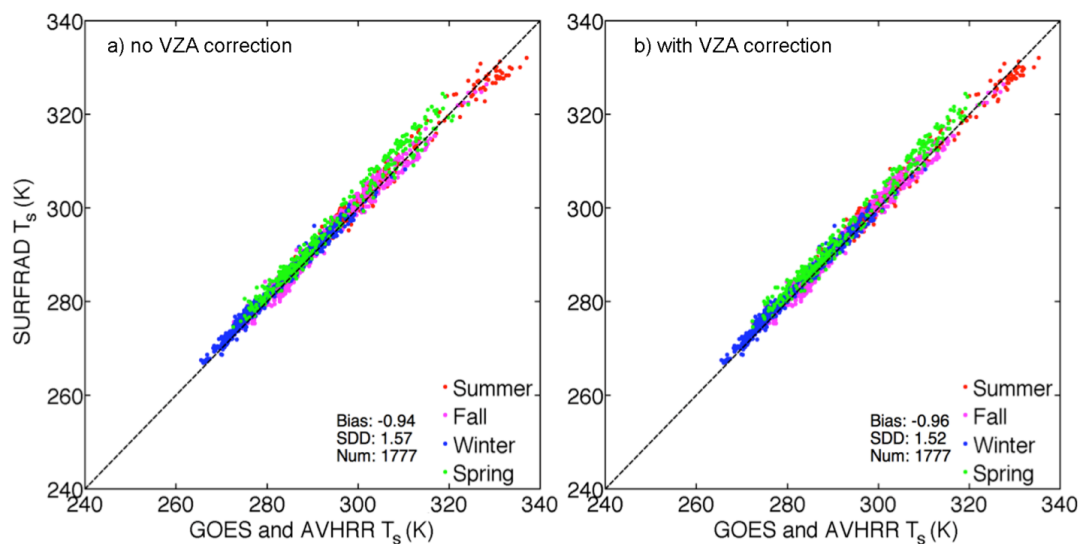


Figure 17: Scatterplots of LST from matched satellite (GOES-13, GOES-15, and AVHRR) and SURFRAD data at Desert Rock, NV, (a) without and (b) with VZA corrections.

5

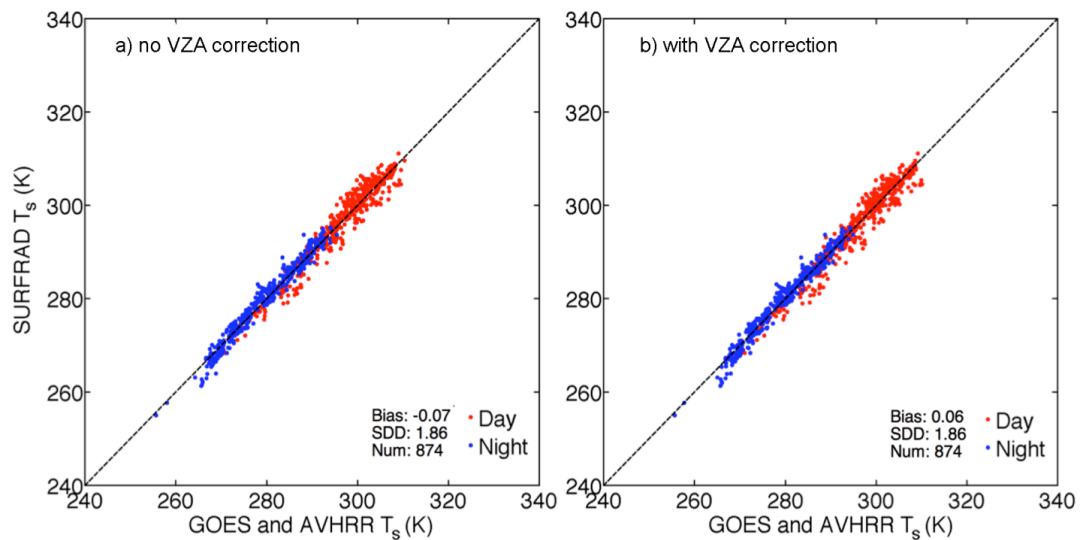


Figure 18: Same as Fig. 17, except for data over Sioux Falls, SD.

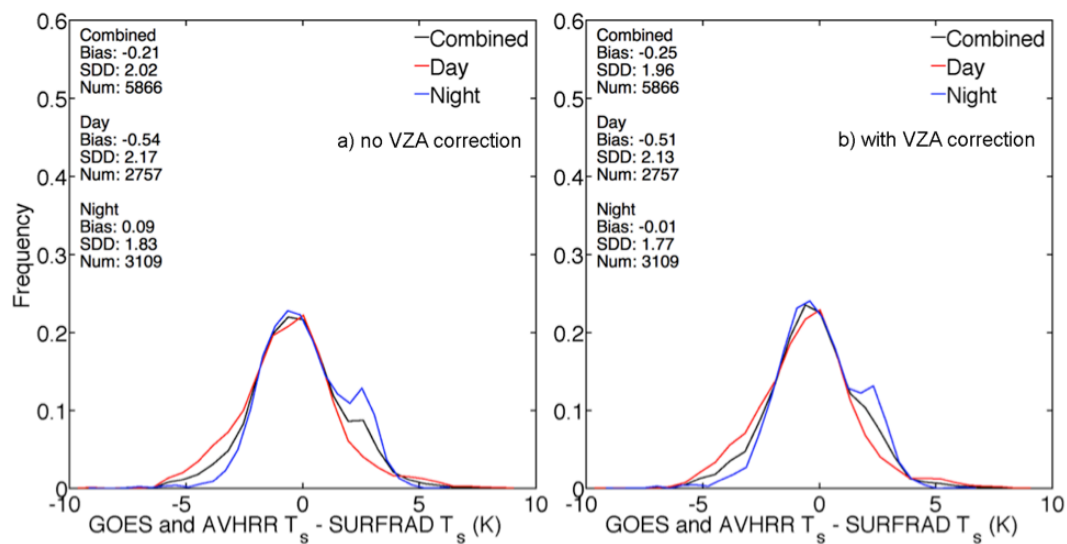


Figure 19: Differences between GOES-13, GOES-15, and AVHRR day, night, and combined LST and SURFRAD LST (a) without and (b) with VZA corrections.